



Repositorio Institucional de la Universidad Autónoma de Madrid

<https://repositorio.uam.es>

Esta es la **versión de autor** del artículo publicado en:

This is an **author produced version** of a paper published in:

Advanced Functional Materials 29.15 (2019): 1808424

DOI: <https://doi.org/10.1002/adfm.201808424>

Copyright: © 2019 WILEY-VCH Verlag GmbH & Co. KGaA, Weinheim

El acceso a la versión del editor puede requerir la suscripción del recurso

Access to the published version may require subscription

3D printing of a thermo- and solvato-chromic composite material based on a Cu(II)-thymine coordination polymer with moisture sensing capabilities

Noelia Maldonado, Verónica G. Vegas, Oded Halevi, Jose Ignacio Martinez, Pooi See Lee Shlomo Magdassi, Michael T. Wharmby, Ana E. Platero-Prats, Consuelo Moreno, Félix Zamora and Pilar Amo-Ochoa**

This paper is dedicated to Esteban and Miguel Zamora-Amo.

N.M, V.G.V., Dr. A. E. P., Dr. C.M., Dr. F.Z., Dr. P.A.O. Departamento de Química Inorgánica, Universidad Autónoma de Madrid, 28049 Madrid, Spain;

O.H., Prof. P.S.L., Prof. S.M. Casali Center for Applied Chemistry, Institute of Chemistry, The Hebrew University of Jerusalem, 91904 Jerusalem, Israel; School of Materials Science and Engineering, Nanyang Technological University, 639798, Singapore; CREATE NTU-HUJ Programme Enterprise Wing, 138602, Singapore;

Dr. J.I.M. Departamento de Nanoestructuras, Superficies, Recubrimientos y Astrofísica Molecular, Instituto de Ciencia de Materiales de Madrid (ICMM-CSIC), 28049 Madrid, Spain;

Dr. M.T.W. Deutsches Elektronen-Synchrotron (DESY), Notkestraße 85, 22607 Hamburg, Germany;

Dr. F.Z., Dr P.A.O. Institute for Advanced Research in Chemical Sciences (IAdChem), Universidad Autónoma de Madrid, 28049 Madrid, Spain;

Dr. F.Z. Condensed Matter Physics Center (IFIMAC), Universidad Autónoma de Madrid, 28049 Madrid,

E-mail: pilar.amo@uam.es

Keywords: coordination polymers, sensing, 3D printing, solvato-thermochromic, water detection

ABSTRACT: This work presents the fabrication of 3D printed composite objects based on copper(II) one-dimensional coordination polymer (**CP1**) decorated with thymine along its chains with potential utility as an environmental humidity sensor and as a water sensor in organic solvents. This new composite object has a remarkable sensitivity, ranging from 0.3 to 4% of water in organic solvents. The sensing capacity is related to the structural transformation due to the loss of water molecules that **CP1** undergoes with temperature or by solvent molecules competition, which induces significant change in color simultaneously. The **CP1** and 3D printed materials are stable in air over one year and also at biological pHs (5-7), therefore suggesting potential applications as robust colorimetric sensor. These results open the door to generate a family of new 3D printed materials based on the integration of multifunctional coordination polymers with organic polymers.

1. Introduction

3D printing is an emerging technology that is expected to bring an industrial revolution in goods manufacturing.^[1] However, in order to realize these expectations, new functional materials for 3D printing are necessary.^[2] Indeed, materials that are feasible for 3D printing are rather limited, being the classical organic polymers with good processability capabilities such as nylon, polypropylene or polycarbonate are among the most popular ones.^[3] While these organic polymers show excellent mechanical and thermal properties, as well as suitable processability under printing conditions, they typically lack functionalities (e.g. electrical/thermal conductivity, luminescence, magnetism, self-healing, etc.) required for various potential applications. Therefore, either the discovery of new functional materials for 3D printing or the integration of known functional materials with printable organic polymers to form suitable functional composites^[4] is a subject of high research and technological interest.^[5]

In this field, coordination polymers (CPs) are well-developed multifunctional materials which are based on the assembly of two building blocks, metal entity and organic ligands, which define both the molecular architecture and properties of the final material. CPs nanostructuring is a relatively new subject, which enables new uses for CPs but also their integration with other materials to produce a new family of (nano)composites. Indeed, very recently, the potential of nanolayers and nanofibers of CP to form multifunctional ultra-thin films was demonstrated.^[6] However despite the high potential for the use of CPs and their porous forms, metal-organic frameworks (MOFs), their use to form new functional materials suitable for 3D printing is limited to just a few examples based on dynamic coordination bonds^[7] and embedding of MOFs within organic and inorganic matrices.^[5b, 8]

Currently, the interest in recognition, quantification and monitoring of important daily-life chemical species is increasing in different fields such as health, food quality control and environmental protection among others. Inexpensive *in situ* fast detection of on-site sensors which respond in a simple and rapid fashion are highly desired. Therefore, it is of current research interest to develop simple and robust sensors with on-site features and to further improve the sensing performance regardless of environmental fluctuations.^[9] A commonly accepted principle for the design of chemosensors is that they must be able to detect substances and produce an easily measurable response, such as a change of color, fluorescence, or of any other macroscopic property.^[10] CPs are excellent candidates for this purpose due to their structural flexibility and dynamic structures, as well as their capability to generate stimuli-responsive materials.^{[11] [12]}

In this work we have fabricated water sensors by printing photopolymerization 3D objects. The printed 3D objects contain embedded nanofibers of the non-toxic,^[13] thermo- and solvatochromic copper(II) one-dimensional coordination polymer grafted with thymine (TAcOH) as a terminal ligand, and 4,4'-bipyridine (4,4'-bipy) as a bridging ligand between the metal centers (**CP1**). This structure includes a coordinated water molecule and two water solvation molecules (**Figure 1**). These water molecules are easily released upon soft-heating or moderate vacuum to produce new related CPs. This is a reversible process that recovers the initial state by the exposure of the materials to water. The water release produces a significant color change in the CP from blue to violet (**Figure 2**) that enables using this compound as a robust moisture humidity sensor^[14] both in air and organic solvents, such as MeOH, EtOH, CH₃CN and THF. In fact, the present non-porous CP is a rare example showing such sensing capability.^[15] In addition, by forming dispersions of **CP1** within photopolymerizable monomers, and a solvent, we have been able to 3D-print different stable composite architectures using a digital light processing (DLP) 3D-printer (**Scheme S1b**) or an extruder

3D-printer (**scheme S1a**). Furthermore, we have shown the ability of these printed materials to detect moisture from air and solvents.

2. Results and Discussion

The direct reaction between $\text{Cu}(\text{NO}_3)_2$ with 4,4'-bipy and TAcOH in water at room temperature leads to the formation of a colloid based on nanofibers of $[\text{Cu}(\text{TAcO})_2(4,4'\text{-bipy})(\text{H}_2\text{O})]_n \cdot 2\text{H}_2\text{O}$ (**CP1**).^[13] The thermal stability of **CP1** powder has been investigated by differential scanning calorimetry (DSC) and thermogravimetric analysis (TGA) coupled to mass spectroscopy (MS)^[16] under O_2 (**Figure S1** and **S2**). Its thermal study shows a first step at 60 °C, indicative of the loss of one water molecule, and a second step at 135 °C indicative of the loss of the two water molecules (**Figure S1**). The heating of **CP1** powder at 60 °C (30 min) results in a significant reversible color change from blue to violet, due to formation of the intermediate material (named **CP1-H₂O**, **Figure 2** in the middle and diffuse reflectance spectra (**Figure S6**, a and b, and **Table S1**)) suggesting that the water molecule lost in the first step could be the one coordinated to the copper. This is a reversible step since cooling **CP1-H₂O** in air, the colour changes from violet to blue, indicating the change to **CP1**. To demonstrate the stability and reproducibility of this process, more than 20 heating cycles at 60 °C and air cooling of **CP1** have been performed, (**Figure S7**). Increasing temperature up to 135 °C for 30 min, an irreversible color change from violet, **CP1-H₂O**, to grayish blue is also observed, **CP1-3H₂O** (**Figure 2** right).

The thermochromism of **CP1** is a reversible process at 60 °C, probably due to the dissociation of the weakly bonded water molecule from the coordination sphere which facilitates a simple structural reorganization. In principle the release of a water molecule coordinated to a metal center seems to be more energetically unfavorable than solvated water molecules, however, this process is supported by X-ray powder diffraction data (**Figure 3**, green line and **Figures S3-S5**) and theoretical modeling (see below and **Figures S8-S10**). Thus, the reversible process of water incorporation into **CP1-H₂O** implies the coordination of a water molecule

back to the copper sphere, regenerating the initial structure **CP1**, upon exposure of **CP1-H₂O** to the moisture of the atmosphere (**CP1-H₂O** under argon does not change to **CP1**). The structural changes in **CP1** seem to be dramatic and irreversible at 135 °C, according to the total loss of the water molecules present in the structure. This agrees with a much pronounced structural change, as is observed in the powder X-ray diffraction data (Figure 3, S3 and S5) and theoretical modeling (see below and Figures S8-S10). We have also studied the behavior of **CP1** at 25 °C in vacuum from 1 h to 4 days, observing a similar color change from blue to violet after 1 h, and to grayish blue after 4 days in vacuum. X-ray powder data were collected for **CP1** at 25 °C in vacuum after 1 h and after 4 days, as well as after heating at 60 and 135 °C for 30 min. Each diffractogram confirmed the structural changes (Figures 3, S3-S5).

2.1. Computational Studies.

In order to understand the obtained experimental data (TGA and the color changes) from the theoretical point of view, we have carried out a DFT-based calculation to compute the transition-state energy barrier for the release of the coordinated water molecule from the structure of the **CP1** (with all the coordinated and solvation water molecules). For that purpose, we have made use of the CI-NEB approach to get a converged MEP taking as first step the optimized all-water molecules **CP1** geometry and an optimized final state with the coordination water molecule removed from the structure, with a total number of intermediate image-states of 20 which were free to relax along the procedure. This calculation yields a transition-state barrier of $\Delta E = 0.63$ eV. On the other hand, the rate for this process has been computed by looking at normal modes possessing amplitudes that make the coordinated water molecule detach from the structure. The rate is then obtained by multiplying the Boltzmann factor (providing the probability to pick up a thermal fluctuation at temperature T to overcome the barrier after “fluctuation”, ΔE) times the number of attempts to pass the barrier given by the frequency of the relevant mode: in this case of around 450 cm^{-1} , $\Gamma = e^{-\frac{\Delta E}{k_B T}}$. In the present case, the values obtained, according the Boltzmann statistics, are consistent with

the loss of the coordination water molecule at 60 °C within minutes, as observed experimentally. In line with the previous data, each solvation water is bound within the system with energy of 1.16 eV. This value is calculated by a difference of total energies between the system with solvation waters, the system without solvation waters and n-times the energy of the water molecules, present in the unit cell. Therefore, to remove the solvation waters, a thermal energy exceeding this cohesion enthalpy is necessary, 1.16 eV per molecule. This can also help to justify the greatest difficulty in losing the solvation water versus the coordination water.

2.2. Pair Distribution Function Studies (PDF).

In addition, to probe the atomic structure of **CP1** after heat treatments and to explore the local structural implications linked to dehydration, we have applied Pair Distribution Function (PDF) analysis based on synchrotron X-ray total scattering data. PDF experiments were carried out on both **CP1** and **CP1-H₂O** samples.

The PDFs for the **CP1** systems are dominated by atom–atom correlations involving the strongly scattering Cu atoms (**Figure 5**). The main PDF contribution is observed at ~ 2.0 Å, which contains correlations from overlapping Cu-N and Cu-O distances associated with the binding 4,4-bipy and TAcO ligands, respectively. PDF data collected on **CP1-H₂O** did not show any significant change on the peak at ~ 2.0 Å, demonstrating that the coordination mode of the ligands to copper remains unaltered during this process.

Interestingly, PDF data collected on the **CP1-H₂O** sample heated at 60 °C showed a subtle decrease in intensity of the PDF peak at ~ 2.3 Å compared to the pristine system. This bond distance is associated with the water molecule bound to the copper as well as carbon-carbon correlations within the ligands. Quantitative analyses of this PDF peak suggested the loss of the Cu-O bonds linked to the dehydration of the copper centers, in agreement with TGA and theoretical calculation data. This result would suggest a change from 5 to 4 coordination number after the heat treatment, which explains the color change experimentally observed.^[14]

Despite the structural transitions, the powder diffraction shows no substantial changes (Figure 3, green line).^[17] After heating at 135 °C, the local structure of **CP1** remains unaltered while major changes are observed at long-range scale. This is also in agreement with the structural transition determined by X-ray powder diffraction analyses (Figure 3 and S5).

2.3. First-principles calculations

Moreover, in order also to investigate the structural and electronic evolution of the **CP1** induced by the sequential loss of the coordinated and solvation water molecules with increasing temperature, we have carried out a series of first-principles calculations. As a starting-point, we have taken the geometry and lattice as obtained from the low-temperature PXRD experiment, where **CP1** has a coordinated water molecule to the Cu atom and two water solvation molecules in the vicinity of the terminal $-\text{CH}_3$ groups of the ligands (Figure 1). Once the structure with all the water molecules is relaxed the resulting structure does not show substantial changes (**Figure S9 and 10**), which indicates the confident performance of our theoretical approach. In a next three-fold step, we have removed from the resulting structure: i) the coordination water molecule, ii) the two solvation water molecules, and iii) the coordination and solvation water molecules simultaneously. All three geometries (i, ii and iii) were again fully relaxed (**Figure S9 and S10**) in order to compare changes with the all-water-molecules case. Consistently with the experimental evidence, the changes in the structure are not very pronounced for the optimized cases i) and ii), where the most noticeable changes are observed in the Cu—N and Cu—O distances decreasing $< 4\%$ for the structure i), and a slight torsion of the $-\text{CH}_3$ terminating groups in the ligands $< 4^\circ$. However, for the case iii), where all the water molecules have been removed before optimizing the structure, the Cu—N and Cu—O distances decrease by around 6% and a rotation of around 8° of the 4,4'-bipyridine units forming the chains is observed.

We have already performed a comparison between the experimental diffractogram for the **CP1** and the simulated power X-ray diffractograms from the DFT-optimized structures with

all water molecules, no solvation water molecules, no coordination water molecule and with any water molecules (Figure S10). Interestingly, the slight geometrical changes observed in all the optimized structures seem not to be sufficiently pronounced to have a clear influence on their correspondingly simulated powder X-ray diffractograms (Figure S10). This finding seems to be consistent with the experimental observations (Figure 3), where the structure of the compounds remains almost locally-unaltered, not much affecting the diffractogram profile. On the other hand, major structural changes are experimentally observed at long-range scale, which, unfortunately, cannot be captured by our theoretical studies. This behavior also agrees with previous related literature reporting on similar systems.^[17]

For the sake of completeness, we have carried out an exhaustive analysis of the computed density of states of the different models that we propose in this study (Figure S9). Figure 6a shows the computed total density of electronic states (in arbitrary units) as a function of the energy referenced to the Fermi energy (in eV) for the **CP1** compound: i) with all the coordination and solvation water molecules, ii) just with the two solvation water molecules, iii) just with the coordination water molecule, and iv) with no water molecules. In a first inspection of this figure we can appreciate that the morphological computed density of electronic states (DOS) profile of the different systems is essentially very similar.

On the other hand, **Figure 6c** shows the computed density of electronic states for the case 6a.i) projected onto: the solvation water molecules, the coordination water molecules, the Cu atoms, the full ligand and onto the full structural chain (Cu atom + 4,4'-bipyridine units). From this figure, the most important information one can extract is the origin and location of the electronic states involved in the first permitted optical transition lying within the visible range, corresponding to the Cu atoms at the Fermi level and the first unoccupied state belonging to the ligands, located at around 2.8 eV above the Fermi level. In order to locate and identify these states in the total density of states, Figure 6b shows the same DOS profiles than in Figure 6a(i-iv) in this case magnified in a reduced energy window between -2 and 6 eV.

In this figure it is possible to identify the low-lying optical transitions between the aforementioned states. The energy difference between these states for the case i) is around 2.7 eV (with all the coordinated and solvation water molecules), whilst this energy is slightly higher for the case ii) of around 2.9 eV (just with the solvation water molecules and the coordinated water molecules removed). This could also justify the experimental observation that the first type of water molecules lost by the **CP1**, corresponding to the coordinated ones, induces a color change from blue to violet (increasing the photon energy). This is also reinforced by the fact that the energy between both states for the case iii) (just with coordinated water molecules) is equal than for case i) with no significant variation in the transition energy. On the other hand, the system at a higher temperature, when all the water molecules are gone, keeps the violet color. This behavior is also observed in the DOS profile for the case iv) of Figure 6b, yielding the same transition energy between these two states as for ii) (of around 2.9 eV). The fact that the energy difference between both specific states is very close to those corresponding to the blue and violet photon energies can be seen here just as a mere anecdote, since the values obtained from conventional DFT must be taken cautiously (conventional DFT underestimate gaps, and within our theory level we are missing excitonic effects). Nonetheless, we can trust the relative positioning of the levels, which in this case agree with the experimental evidence.

2.4. Humidity Sensor.

The determination of low quantities of water in organic solvents or in the atmosphere is of importance for numerous industrial and scientific applications.^[11b] The most common analytical procedure for water detection in solvents is the Karl-Fischer titration. This method has some disadvantages such as the requirement for special equipment, complicated sample manipulations and trained lab staff.^[18] Therefore, visual sensing devices with low detection limits and sensitivities similar to those provided by the Karl Fischer titration are a reasonable alternative for humidity detection in solvents. There have been some studies on composite

materials,^[19] electrolytes, polymers,^[20] and fluorescent materials^[21] that have been utilized to detect low amounts of water in solvents.^[22] However, there are just few examples of porous coordination polymers (MOFs)^[11b, 12, 23] and almost none that we know based on non-porous coordination polymers.

In order to study the atmospheric relative humidity (RH) detection capacity of dehydrated violet **CP1-H₂O**, the sample was placed in a dry box under an argon atmosphere and exposed to controlled relative humidity (RH) ranging from 6.5% RH (relative humidity inside the dry box at 25 °C) to a gradually increased 9.2% RH. A change in color from violet to blue was observed at 7% RH due to rehydration of **CP1-H₂O** to **CP1** (**Figure 7**).

2.4.1. Water Detection Limit (LOD) of CP1 and CP1-H₂O in dry organic solvents.

We have studied the detection capacity of **CP1** and **CP1-H₂O** materials under wet conditions. For these experiments we have soaked both **CP1** and **CP1-H₂O** in a variety of dry organic solvents to test its changes in color at room temperature and under atmospheric conditions. In these experiments, ethanol (EtOH, 99.5%), methanol (MeOH, 99.9%), acetonitrile (CH₃CN, 99.8%) and tetrahydrofuran (THF, 99.9 %) (**Figure 8**) were tested. In all cases, the changes are reversible and takes few minutes (from 1 to 15 min).

Thus, when **CP1** is soaked in dry MeOH or EtOH, the material immediately changes its color from blue to violet (1 min.) (diffuse reflectance spectra, **Figure S6, c and d** and **Table S1**) . Once the organic solvent is removed, just upon allowing it to evaporate in air, the RH of the ambient (*ca.* 20%) is able to interchange the solvent molecules and turning it back to the blue **CP1** in less than 2 min. We assume that soaking **CP1** in MeOH produces a ligand exchange between the copper coordinated water molecule and the MeOH that is reversed in the presence of water molecules of the ambient to **CP1**. This reversible process has also been tested using EtOH, THF and acetonitrile with similar results (**Figure 8**).

In order to confirm the ligand exchange in **CP1** after soaking in dry organic solvents, we have confirmed that after immersion of **CP1** for 2 min in EtOH at 25 °C the color changes from blue to violet and the X-ray powder diffractogram also changes significantly (**Figure 9**).

The solvatochromism property of the **CP1** may be due to the dissociation of the weakly bonded water molecule from the coordination sphere which facilitates the approach of the solvent molecules above and below the plane to the copper(II) center.^[24] This is corroborated by conducting the experiment in dry organic solvents starting from the violet **CP1-H₂O**, obtaining similar results (**Table 1**).

To study the capacity of water detection in dry organic solvents of **CP1** and **CP1-H₂O** the bulk materials were exposed to different organic almost dry solvents, ethanol 99.5%, methanol 99.95%, tetrahydrofuran 99.9% and acetonitrile 99.8%. All the experiments were carried out at room temperature. A well-known volume of solvent was added over an amount of the coordination polymer. In case of **CP1**, when the compound changed its color to violet, water was added in small volumes (~5 µL) until the coordination polymer changed to blue again. Finally, the detection limit (LOD) was calculated in percentage (**Table 1**). In case of **CP1-H₂O** which starts as a violet material, we did not observe any initial color change and after 30 min. water was added in small volumes until the coordination polymer changed to blue again. The results show that **CP1** is more sensitive to water than **CP1-H₂O**.

2.5. 3D printing of compound **CP1**.

For practical applications of **CP1**, 3D-printing techniques have been utilized to form a variety of architectures (**Figure 10**). In order to form a 3D printable ink, while taking into account the low toxicity of **CP1** toward cells^[13] and its stability at physiological pH; considering the idea that it can also be applied in biologically related devices, **CP1** was dispersed within a biodegradable monomer, dipropylene glycol diacrylate (SR-508). In addition to SR-508, another monomer, ethoxylated trimethylolpropane triacrylate (SR-9035), a solvent, diethylene glycol methyl ether (DM), and photoinitiators (Irgacure 819 and 184) were added to form the

stable polymerizable 3D printable ink. By utilizing 3D printing to embed the **CP1** powder within a matrix (**CP1@3D**), it is easier to handle, while the mechanical properties of the printed object can be tailored according to the chosen monomers. Two formulations were composed to give **CP1@3D** structures with 10 wt% and 40 wt% of **CP1**. These were 3D printed using a digital light processing (DLP) printer and an extruding printer, respectively. The extruding printer was used for the 40 wt% formulation due to the high viscosity of the ink that did not enable its printing via DLP. The samples were printed in different shapes (Figure 10a-c) with a maximum level of resolution of 200 μm , achieved with the DLP printer. The printed composites were characterized by X-ray powder diffraction (**Figure S11**) and scanning electron microscopy (SEM) (**Figure 10d-f**). The 3D printed objects contain the nano- and submicrometric fibers of the starting polymer (**CP1**), distributed homogeneously within the polymeric matrix (Figure 10d-f).

2.5.1. Sensing studies on **CP1@3D**.

To evaluate the water detection limit (LOD) of the activated 3D printed composite objects, **CP1@3D**, and compare it with **CP1** and **CP1-H₂O**, similar experiments have been carried out with **CP1@3D** using different dry organic solvents, *i.e.* ethanol 99.5%, methanol 99.95 %, tetrahydrofuran 99.9% and acetonitrile 99.8% (**Figure 11**). The data obtained (Table 1), show that the new 3D-printed objects (**CP1@3D**) has a detection capacity very similar to that of **CP1**, with the advantage that we can adapt its form to any shape of device.

The color change of the **CP1@3D** from blue to violet has been obtained even after 20 cycles heating at 60 °C and air cooling, powder X-ray diffraction spectra confirm the stability of the compound (Figure S7).

As for the powdered samples, we performed the study in a dry box in order to evaluate the ability to detect the relative humidity (RH) of the air with the 3D printed material. In this case, the printed material seems to be more sensitive than the **CP1**, detecting relative humidity below 6.5%. This is probably due to the fact that the new 3D printed material is a composite

composed of an organic matrix of glycolic nature, with certain hygroscopic character and porosity. This evidence could explain that the color change from violet to blue occurs faster for **CP1@3D** than for pristine **CP1-H₂O**.

3. Conclusions

We have previously shown the potential biological interest of $[\text{Cu}(\text{TAcO})_2(4,4'\text{-bipy})(\text{H}_2\text{O})]_n \cdot 2\text{H}_2\text{O}$ because of the presence of the thymine moiety along the chains of this coordination polymer and the simple way to produce nanofibres of this material in a one-pot procedure ^[13]. Now we show the ability of **CP1** to selectively lose water molecules from its structure and generate two new CPs. In a first step, at moderate temperature (60 °C) or under vacuum, **CP1** releases one water molecule with a significant change in color, from blue to violet, reversibly, giving rise to the formation of **CP1-H₂O**. Although it is counterintuitive, the first water molecule that is released in this process, is the one coordinated to the copper atom in **CP1**. This process has been carefully analyzed with the help of theoretical calculations and advanced X-ray techniques.

We have confirmed the use of this reversible thermochromic transformation, from **CP1** to **CP1-H₂O**, to detect moisture in air and solvents. In addition, the easy preparation of **CP1** in colloidal form as nanofibers has enabled its formulation as inks that can be 3D printed. This enables us to fabricate **CP1@3D** in a variety of architectures, useful for detection of moisture in several organic solvents. It is remarkable that 3D printing of **CP1@3D** may allow the production of almost any desired shape required for a given application and fabricate different devices.

This work shows the first 3D printed composite objects created from a non-porous coordination polymer and opens the door to the use of this large family of compounds that are easy to synthesize and exhibit interesting magnetic, conductive and optical properties, in the field of functional 3D printing.

4. Experimental Section

Materials and Methods. All reagents and solvents were purchased from standard chemical suppliers: Thymine-1-acetic (TAcOH) acid 98% Sigma-Aldrich; 4,4'-Dipyridyl (4,4-bipy) 98% Sigma-Aldrich; Copper nitrate trihydrate extra pure Scharlab; potassium hydroxide Scharlab; Dipropylene glycol diacrylate (DPGDA, SR-508) Sartomer; Ethoxylated trimethylolpropane triacrylate (SR-9035) Sartomer; Diethylene glycol methyl ether (DM) $\geq 99.0\%$ Sigma-Aldrich; Irgacure 819 BASF; Irgacure 184 BASF; ethanol (EtOH, 99.5%), methanol (MeOH, 99.95%), acetonitrile (CH₃CN, 99.8%) and tetrahydrofuran (THF, 99.9%) and used as received.

Infrared (IR) spectra were recorded on a PerkinElmer 100 spectrophotometer using a PIKE Technologies MIRacle Single Reflection Horizontal ATR Accessory from 4000–600 cm⁻¹.

Elemental analysis were performed on an elementary microanalyzer LECO CHNS-932. It works with controlled doses of O₂ and a combustion temperature of 1000 °C.

Powder X-ray diffraction has been collected using two different equipments. The first one Diffractometer PANalyticalX'Pert PRO MPD $\theta/2\theta$ secondary monochromator and detector with fast X'Celerator, it is used to general assays. The second one is a Diffractometer PANalyticalX'Pert PRO ALPHA1 $\theta/2\theta$ primary monochromator and detector with fast X'Celerator, which is used to analyse immersed samples in a solvents or under an inert atmosphere. The immersed samples were prepared on a silicon sample holder and covered with a sheet of kapton and the samples under nitrogen were prepared on a silicon sample holder too with polycarbonate sealing cap. Theoretical X-ray powder diffraction patterns were calculated using Mercury Cambridge Structural Database (CSD) version 3.10 software from the Crystallographic Cambridge Data Base (CCDC). The samples have been analysed with scanning $\theta/2\theta$.

Thermogravimetric analysis (TGA) was performed on a TGA Q500 Thermobalance with an EGA (Envolved Gas Analysis) furnace and quadrupole mass spectrometer Thermostat Pfeiffer of Tecnovac, to analyse gases which are given off from the sample. The powder sample was analysed using a Pt sample holder and O₂ flow as purge gas of 90 mL/min with a heating ramp from room temperature to 1000 °C at 10 °C /min.

Differential Scanning Calorimetry (DSC) was performed on a Discovery DSC. The sample was analysed using hermetic Aluminium pans from 20 °C to 200 °C in a N₂ atmosphere with two heating rate of 5 °C /min and 10 °C/min.

Field emission scanning electron microscopy (FESEM) images were recorded on a Philips XL30 S-FEG field emission scanning electron microscope, and on Carl Zeiss SUPRA 55 scanning electron microscope.

Diffuse Reflectance studies (DR) StellarNet spectrophotometer model Blue-Wave, with internal slot of 25 μ m and diffraction network of 600 lines/mm, equipped with fiberglass both

for illumination and for capturing the reflected light. With diffuse reflectance probe R400-7-VISNIR and StellaNet lamp light source model SL1. White RS50 reflectance pattern from StellarNet. Range of wavelengths of 350-2200nm.

The diffuse reflectance measurements have been taken in a 45°/45° illumination/detection configuration, with respect to the sample surface. Each measurement consists of an average of 5 spectra of 200 ms, 5 different measurements are made, so that each signal is composed of the average of 25 spectra of 200 ms. The software used to make the measurements is SpectraWiz program & apps, from StellarNet. Diffuse reflectance measurements are represented by two graphs, the reflectance (% diffuse reflectance) and the remission function (F (diffuse reflectance)) versus wavelength. The remission function is determined by the Kubelka-Munk equation. The collected data is treated with Origin 9.0 to get to the graphic representations that appear in the supplementary material. (**Figure S6**).

Synchrotron X-ray total scattering data suitable for Pair Distribution Function (PDF) analyses were collected at the P02.1 beamline at PETRA III using 60 keV (0.207 Å) X-rays. Samples were loaded into borosilicate capillaries and sealed using epoxy. Data were collected using an amorphous silicon-based PerkinElmer detector area detector. Geometric corrections and reduction to one-dimensional data used DAWN Science software.^[25] PDFs were obtained from the data within PDFgetX3^[26] within xPDFsuite to a $Q_{\text{max}} = 17 \text{ Å}^{-1}$. Cu-N,O correlations of interest were quantified by fitting Gaussian functions.

Theoretical Modeling and Computational details

All the first-principles simulations have been performed by using density functional theory (DFT) as implemented in the CASTEP simulation package.^[27] Exchange–correlation interactions have been accounted by the generalized gradient approximation (GGA) within the Perdew-Burke-Ernzerhof (PBE) functional,^[28] which are based on a total energy pseudo-potential plane-wave framework.^[29] The Vanderbilt ultrasoft pseudopotential scheme has been adopted to model the ion-electron interactions, and the valence atomic configurations

considered are the following: H: $1s^1$, C: $2s^2 2p^2$; N: $2s^2 2p^3$, O: $2s^2 2p^4$, and Cu: $3d^{10} 4s^1$. The cutoff energy has been set to 380 eV, an optimal k -point mesh of $[6 \times 3 \times 1]$ and a self-consistent field (SCF) of 1×10^{-6} eV per atom are used for geometry optimizations using the Monkhorst–Pack scheme.^[30] Full geometry optimizations, where all the atoms are free to relax, have been carried out before single-point energy calculations and the final net force acting on each atom is less than $0.05 \text{ eV } \text{\AA}^{-1}$, the final stress on the atoms is below 0.05 GPa. Transition-state barriers have been computed within the Climbing-image Nudged-elastic-band (CI-NEB) approach,^[31] where the initial and final steps, as well as a sufficient number of intermediate images (20 in this case), have been permitted to fully relax to achieve a converged Minimum Energy Path (MEP). To check the reliability of the results, additional test-calculations with a higher plane-wave cutoff energy and a denser k -point grid were performed, yielding no significant changes for both geometric and electronic structures, and obtaining differences between total energies $< 0.02\%$, which justifies the validity of our calculations. The theoretical crystal-powder diffractograms have been simulated from the DFT-optimized structures by using the MERCURY package.^[32]

Synthesis of the $[\text{Cu}(\text{TAcO})_2(4,4'\text{-bipy})(\text{H}_2\text{O})]_n \cdot 2\text{H}_2\text{O}$ (CP1) and CP1@135 °C

The synthesis of this coordination polymer **CP1** has already been reported by *G. Vegas et al.*^[13]

The **CP1@135 °C** was obtained by heating **CP1** during 20 minutes at 135 °C, this new emerged structure was characterized by IR selected data (cm^{-1}): 3165 (w), 3050 (w), 2823 (w), 1689 (s), 1612 (s), 1630 (m), 1463 (m), 1418 (m), 1377 (m), 1300 (m), 1278 (m), 1246 (m), 1228 (m) and Elementary Analysis for $\text{C}_{24}\text{H}_{22}\text{CuN}_6\text{O}_8$, Calcd. (Found): %C, 49.2 (48.9); %N, 14.3 (14.2); %H, 3.8 (3.9).

Preparation of the Printing Formulation: 1) 10% wt- $[\text{Cu}(\text{TAcO})_2(4,4'\text{-bipy})(\text{H}_2\text{O})]_n \cdot 2\text{H}_2\text{O}$ (2 g) was mixed with DPGDA (9 g), Sr-9035 (9 g) and DM (4 g) as a solvent. To form a homogeneous dispersion, the mixture was sonicated with a tip-sonicator

(Sonics Vibra-cell, 500 W) for 45 min (1 s ON, 2 s OFF) and 50% amplitude. Following this, photoinitiators, Irgacure 819 (0.16 g) and Irgacure 184 (0.32 g), were dissolved in the dispersion. 2) **40% wt-** $[\text{Cu}(\text{TAcO})_2(4,4'\text{-bipy})(\text{H}_2\text{O})]_n \cdot 2\text{H}_2\text{O}$ (2.26 g) was mixed with DPGDA (1.65 g), SR-9035 (1.65 g) and DM (4.44 g) as a solvent. To form a homogeneous dispersion, the mixture was mixed with a homogenizer (IKA T25) for 5 minutes and 5000 RPM. Following this, photoinitiators, Irgacure 819 (0.07 g) and Irgacure 184 (0.14 g), were dissolved in the dispersion.

3D-printing of $[\text{Cu}(\text{TAcO})_2(4,4'\text{-bipy})(\text{H}_2\text{O})]_n \cdot 2\text{H}_2\text{O}$ (CP1@3D) embedded with polymeric structures

The models containing 10% wt $[\text{Cu}(\text{TAcO})_2(4,4'\text{-bipy})(\text{H}_2\text{O})]_n \cdot 2\text{H}_2\text{O}$ were printed with a digital light processing (DLP) 3D-printer (Asiga Pico2) (scheme S1a). The models containing 40% wt $[\text{Cu}(\text{TAcO})_2(4,4'\text{-bipy})(\text{H}_2\text{O})]_n \cdot 2\text{H}_2\text{O}$ were printed with an extruder 3D-printer (Hyrel System 30M) (scheme S1b). In both printers, the polymerization was initiated by ultra-violet (UV) light, with a wavelength of 400-405 nm. Following the printing process, the objects were washed with isopropyl alcohol to remove the unpolymerized residues.

Supporting Information

Supporting Information is available from the Wiley Online Library or from the author.

Acknowledgements

The authors thank financial support from the Spanish Ministerio de Economía y Competitividad (MAT2016-77608-C3-1-P, MAT2016-75883-C2-2-P), and the National Research Foundation, Prime Minister's Office, Singapore under its Campus for Research Excellence and Technological Enterprise (CREATE) programme. O.H acknowledges the support for PhD students from The Hebrew University of Jerusalem. J.I.M. acknowledges the financial support by the "Ramón y Cajal" Program of MINECO (Grant RYC-2015- 17730) and the EU via the ERC-Synergy Program (Grant ERC- 2013-SYG-610256

NANOCOSMOS). A.E.P.P. acknowledges a TALENTO grant (2017-T1/IND5148) from Comunidad de Madrid. We acknowledge DESY (Hamburg, Germany), a member of the Helmholtz Association HGF, for the provision of experimental facilities. Parts of this research were carried out at beamline P02.1 PETRA III under the proposal I-20170717 EC. The authors thank to Deseada Diaz Barrero, from Autonoma University of Madrid, Applied Physics Department, the study of diffuse reflectance of the compound presented here. Noelia Maldonado and Verónica G. Vegas, contributed equally to this work.

Received: ((will be filled in by the editorial staff))

Revised: ((will be filled in by the editorial staff))

Published online: ((will be filled in by the editorial staff))

References

- [1] a) L. Pugliese, S. Marconi, E. Negrello, V. Mauri, A. Peri, V. Gallo, F. Auricchio, A. Pietrabissa, *Updates Surg.* **2018**, *70*, 381; b) M. Kuehnel, T. Froehlich, R. Fuessl, M. Hoffmann, E. Manske, I. W. Rangelow, J. Reger, C. Schaeffel, S. Sinzinger, J. P. Zoellner, *Meas. Sci. Techn.* **2018**, *29*, 114002; c) Z. Zhu, S. Z. Guo, T. Hirdler, C. Eide, X. Fan, J. Tolar, M. C. McAlpine, *Adv. Mater.* **2018**, *30*, 1707495; d) H. Yuan, K. Xing, H. Y. Hsu, *Bioengineering* **2018**, *5*, 57. e) W. Gutierrez-Sandi, T. Lemos-Pires, G. Carlo Galiano-Murillo, J. Alejandro Madrigal-Lobo, *Tecnologia En Marcha* **2018**, *31*, 131.
- [2] a) K. D. Roehm, S. V. Madihally, *10*, 015002; b) S. T. Bendtsen, M. Wei, *Journal of J. Biomed. Ma. Res. A* **2017**, *105*, 3262; c) H. Ma, J. Luo, Z. Sun, L. Xia, M. Shi, M. Liu, J. Chang, C. Wu, *Biomaterials* **2016**, *111*, 138.
- [3] a) E. J. Mott, M. Busso, X. Luo, C. Dolder, M. O. Wang, J. P. Fisher, D. Dean, *Mater. Sci. Eng. C* **2016**, *61*, 301; b) A. Al Mousawi, F. Dumur, P. Garra, J. Toufaily, T. Hamieh, F. Goubard, B. Thanh-Tuan, B. Graff, D. Gignes, J. P. Fouassier, J. Lalevee, *J. Polym. Sci., Part A: Polym. Chem.* **2017**, *55*, 1189; c) S. J. Lee, D. Lee, T. R. Yoon, H. K. Kim, H. H. Jo, J. S. Park, J. H. Lee, W. D. Kim, I. K. Kwon, S. A. Park, *Acta Biomater.* **2016**, *40*, 182.
- [4] X. Li, Y. Wang, Z. Wang, Y. Qi, L. Li, P. Zhang, X. Chen, Y. Huang, *Macromol. Biosci.* **2018**, *18*, 1800068.
- [5] a) P. Li, H. Yu, N. Liu, F. Wang, G. B. Lee, Y. Wang, L. Liu, W. J. Li, *Biomater. Sci.* **2018**, *6* (6), 1371; b) O. Halevi, J. M. R. Tan, P. S. Lee, S. Magdassi, *Adv. Sustainable Syt.* **2018**, *2*, 1700150.
- [6] a) J. Troyano, O. Castillo, J. I. Martínez, V. Fernández-Moreira, Y. Ballesteros, D. Maspoch, F. Zamora, S. Delgado, *Adv. Funct. Mater.* **2018**, *28*, 1704040. b) J. Conesa-Egea, J. Gallardo-Martínez, S. Delgado, J. I. Martínez, J. Gonzalez-Platas, V. Fernández-Moreira, U. R. Rodríguez-Mendoza, P. Ocón, F. Zamora, P. Amo-Ochoa, *Small* **2017**, *13*, 1700965; c) J. Conesa-Egea, N. Nogal, J. I. Martínez, V. Fernández-

- Moreira, U. R. Rodríguez-Mendoza, J. González-Platas, C. J. Gómez-García, S. Delgado, F. Zamora, P. Amo-Ochoa, *Chem. Sci.* **2018**, *9*, 8000.
- [7] a) J. C. Lai, L. Li, D. P. Wang, M. H. Zhang, S. R. Mo, X. Wang, K. Y. Zeng, C. H. Li, Q. Jiang, X. Z. You, J. L. Zuo, *Nat. Commun.* **2018**, *9*, 2725; b) L. Shi, H. Carstensen, K. Hoelzl, M. Lunzer, H. Li, J. Hilborn, A. Ovsianikov, D. A. Ossipov, *Chem. Mater.* **2017**, *29*, 5816.
- [8] a) H. Thakkar, S. Eastman, Q. Al-Naddaf, A. A. Rownaghi, F. Rezaei, *ACS Appl. Mater. Interfaces* **2017**, *9*, 35908; b) M. C. Kreider, M. Sefa, J. A. Fedchak, J. Scherschligt, M. Bible, B. Natarajan, N. N. Klimov, A. E. Miller, Z. Ahmed, M. R. Hartings, *Polym. Adv. Technol.* **2018**, *29*, 867.
- [9] J. Deng, F. Wu, P. Yu, L. Mao, *Appl. Mater. Today* **2018**, *11*, 338.
- [10] O. S. Wenger, *Chem. Rev.* **2013**, *113*, 3686.
- [11] a) H. Hosokawa, T. Mochida, *Langmuir* **2015**, *31*, 13048; b) S. S. Nagarkar, S. K. Ghosh, *J. Chem. Sci.* **2015**, *127*, 627; c) S.-i. Noro, N. Yanai, S. Kitagawa, T. Akutagawa, T. Nakamura, *Inorg. Chem.* **2008**, *47*, 7360.
- [12] A. Douvali, A. C. Tsipis, S. V. Eliseeva, S. Petoud, G. S. Papaefstathiou, C. D. Malliakas, I. Papadas, G. S. Armatas, I. Margiolaki, M. G. Kanatzidis, T. Lazarides, M. J. Manos, *Angew. Chem. Int. Ed.* **2015**, *54*, 1651.
- [13] V. G. Vegas, R. Lorca, A. Latorre, K. Hassanein, C. J. Gómez-García, O. Castillo, Á. Somoza, F. Zamora, P. Amo-Ochoa, *Angew. Chem. Int. Ed.* **2017**, *56*, 987.
- [14] M. G. Amiri, H. Golchoubian, *J. Mol. Struct.* **2018**, *1165*, 196.
- [15] a) A. Kobayashi, H. Hara, S.-i. Noro, M. Kato, *Dalton Trans.* **2010**, *39*, 3400; b) H. Hara, A. Kobayashi, S. i. Noro, H. C. Chang, M. Kato, *Dalton Trans.* **2011**, *40*, 8012; c) A. Dey, A. Garai, V. Gude, K. Biradha, *Cryst. Growth Des.* **2018**, *18*, 6070.
- [16] C. Näther, J. Greve, I. Jeß, *Chem. Mater.* **2002**, *14*, 4536.
- [17] A. E. Platero-Prats, A. Mavrandonakis, L. C. Gallington, Y. Liu, J. T. Hupp, O. K. Farha, C. J. Cramer, K. W. Chapman, *J. Am. Chem. Soc.* **2016**, *138*, 4178.
- [18] C. Harris, *Talanta* **1972**, *19*, 1523.
- [19] a) Y. Sadaoka, M. Matsuguchi, Y. Sakai, *Sens. Actuators A: Phys.* **1991**, *26*, 489; b) Y. Itagaki, S. Nakashima, Y. Sadaoka, *Sens. Actuators B: Chem.* **2009**, *142*, 44; c) S. Sohrabnezhad, A. Pourahmad, M. A. Sadjadi, *Mater. Lett.* **2007**, *61*, 2311; d) N. A. Luechinger, S. Loher, E. K. Athanassiou, R. N. Grass, W. J. Stark, *Langmuir* **2007**, *23*, 3473; e) D. Bridgeman, J. Corral, A. Quach, X. Xian, E. Forzani, *Langmuir* **2014**, *30*, 10785.
- [20] E. Kim, S. Y. Kim, G. Jo, S. Kim, M. J. Park, *CS Appl. Mater. Interfaces* **2012**, *4*, 5179.
- [21] J. C. Tellis, C. A. Strulson, M. M. Myers, K. A. Kneas, *Anal. Chem.* **2011**, *83*, 928.
- [22] a) C. P. L. Rubinger, C. R. Martins, M. A. De Paoli, R. M. Rubinger, *Sens. Actuators B: Chem.* **2007**, *123*, 42; b) Y. Li, M. J. Yang, N. Camaioni, G. Casalbore-Miceli, *Sens. Actuators B: Chem.* **2001**, *77*, 625; c) K. S. Chou, T. K. Lee, F. J. Liu, *Sens. Actuators B: Chem.* **1999**, *56*, 106; d) M. M. F. Choi, O. Ling Tse, *Anal. Chim. Acta* **1999**, *378*, 127; e) Z. Wang, J. Zhang, J. Xie, C. Li, Y. Li, S. Liang, Z. Tian, T. Wang, H. Zhang, H. Li, W. Xu, B. Yang, *Adv. Funct. Mater.* **2010**, *20*, 3784; f) M. M. Hawkeye, M. J. Brett, *Adv. Funct. Mater.* **2011**, *21*, 3652.
- [23] a) K. Müller-Buschbaum, F. Beuerle, C. Feldmann, *Microporous Mesoporous Mater.* **2015**, *216*, 171; b) Y. Yu, J. P. Ma, Y. B. Dong, *CrystEngComm* **2012**, *14*, 7157; c) Z. Hu, B. J. Deibert, J. Li, *Chem. Soc. Rev.* **2014**, *43*, 5815.
- [24] H. Golchoubian, R. Samimi, *Polyhedron* **2017**, *128*, 68-75.
- [25] M. Basham, J. Filik, M.T. Wharmby, P.C.Y. Chang, B. El Kassaby, M. Gerring, J. Aishima, K. Levik, B.C.A. Pulford, I. Sikharulidze, *J. Synchrotron Rad.* **2015**, *22*, 853-858.

- [26] C. L. F. P. Juhás, T. Davis, S. J. L. Billinge, *J. Appl. Cryst.* **2013**, *46*, 560.
 [27] M. D. Segall, J. D. L. Philip, M. J. Probert, C. J. Pickard, P. J. Hasnip, S. J. Clark, M. C. Payne, *J. Phys: Cond. Matter* **2002**, *14*, 2717.
 [28] J. P. Perdew, K. Burke, M. Ernzerhof, *Phys. Rev. Lett.* **1996**, *77*, 3865.
 [29] D. Vanderbilt, *Phys. Rev. B* **1990**, *41*, 7892.
 [30] H. J. Monkhorst, J. D. Pack, *Phys. Rev. B* **1976**, *13*, 5188.
 [31] B. J. Berne, G. Cicotti, D. F. Coker, *World Scientific Publishing Company*, Singapore **1998**.
 [32] I. J. B. C. F. Macrae, J. A. Chisholm, P. R. Edgington, P. McCabe, E. Pidcock, L. Rodriguez-Monge, R. Taylor, J. van de Streek, P. A. Wood, *J. Appl. Cryst.* **2008**, *41*, 466.

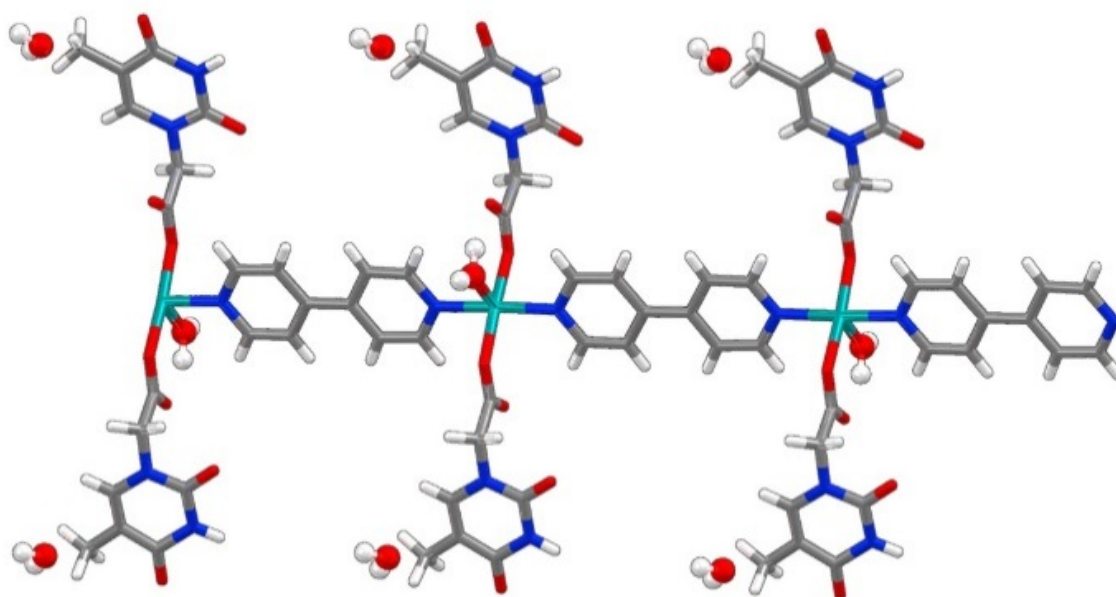


Figure 1. View of a chain of $[\text{Cu}(\text{TAcO})_2(\text{H}_2\text{O})(4,4'\text{-bipy})]_n \cdot 2\text{H}_2\text{O}$. Oxygen atoms are in red, copper atoms are in green, nitrogen atoms are in blue, carbons atoms are in grey and hydrogen atoms are in white.

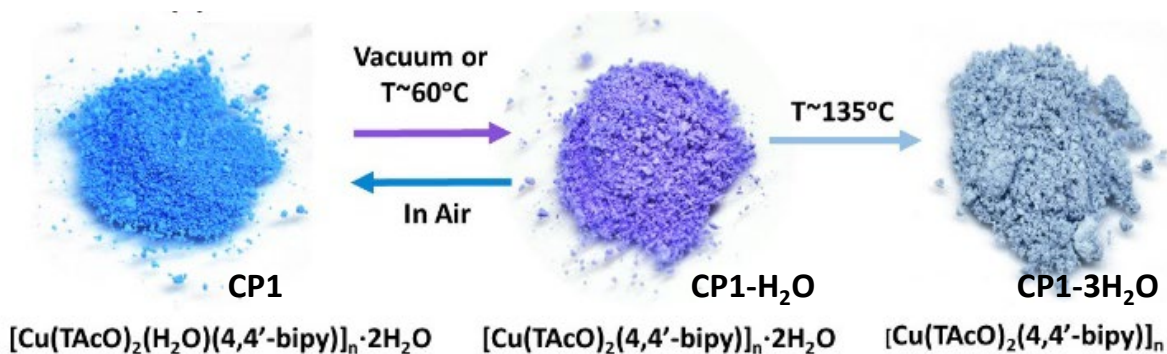


Figure 2. Photos of the corresponding powders in the transformation process mediated by either temperature or vacuum from **CP1** to **CP1-H₂O** and from **CP1-H₂O** to **CP1-3H₂O**.

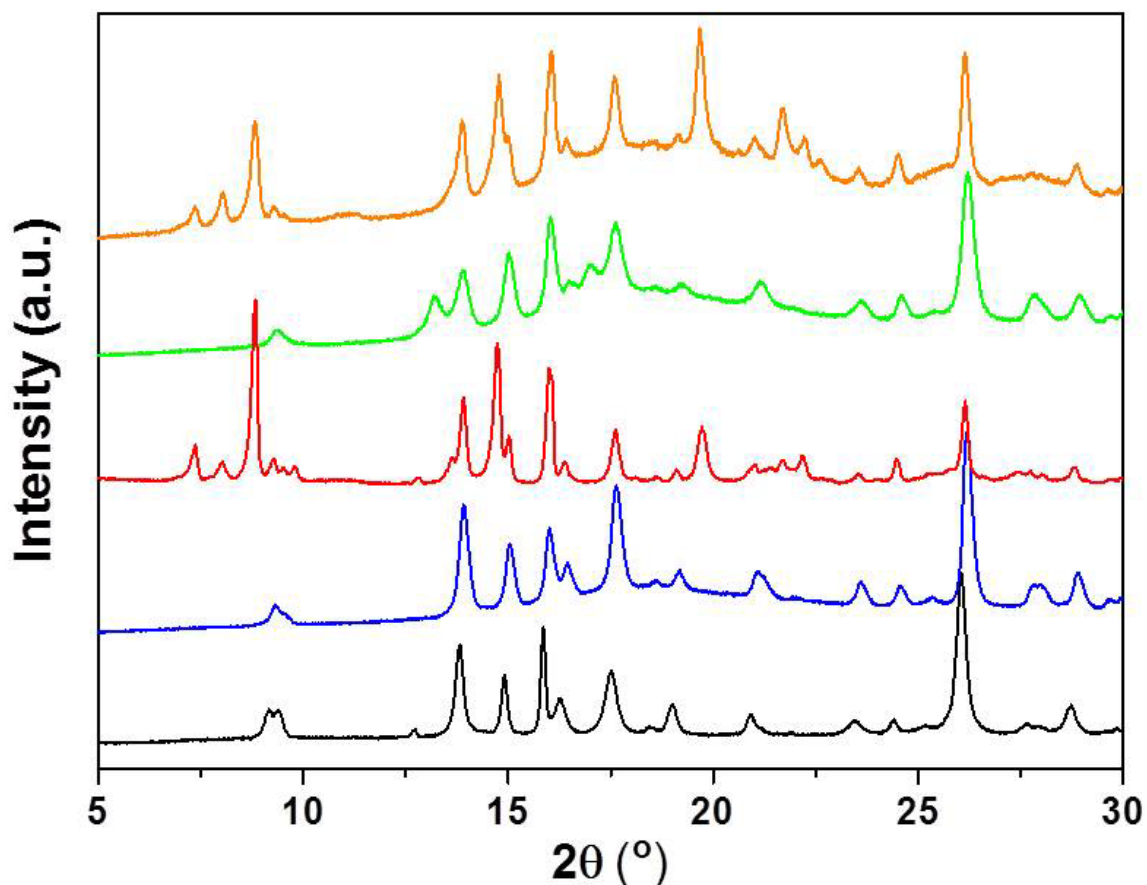


Figure 3. X-ray powder diffraction patterns of CP1 as bulk powder under ambient conditions (black line), CP1 after 1 hour under vacuum (blue line), CP1 after 4 days under vacuum (red line), CP1 after heating in argon atmosphere at 60 °C for 30 minutes (green line), and CP1 after heating at 135 °C for 30 minutes (orange line).

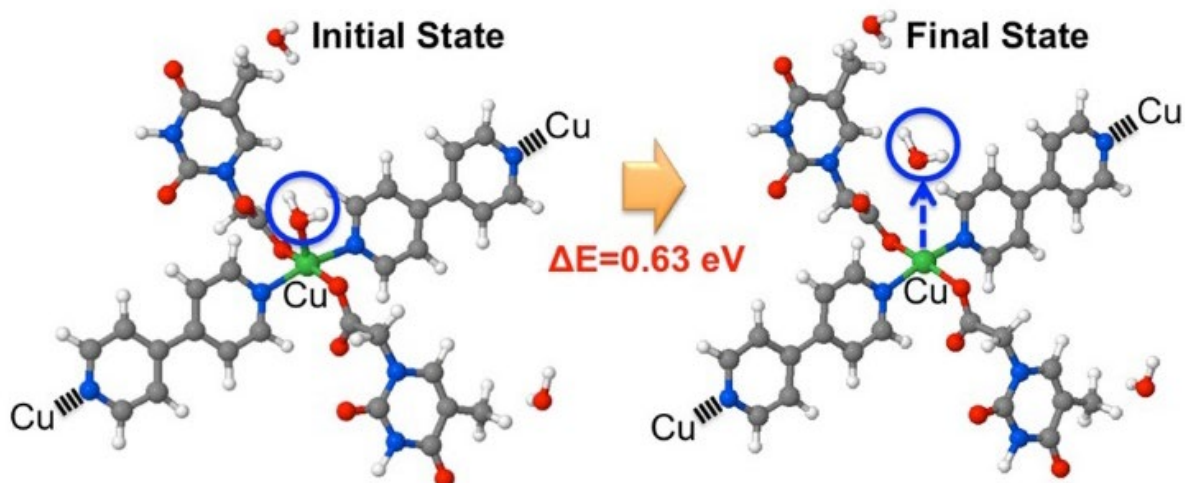


Figure 4. Optimized initial and final state for the computation of the transition-state energy barrier for the release of the coordinated water molecule from the CP1 structure within the CI-NEB approach.

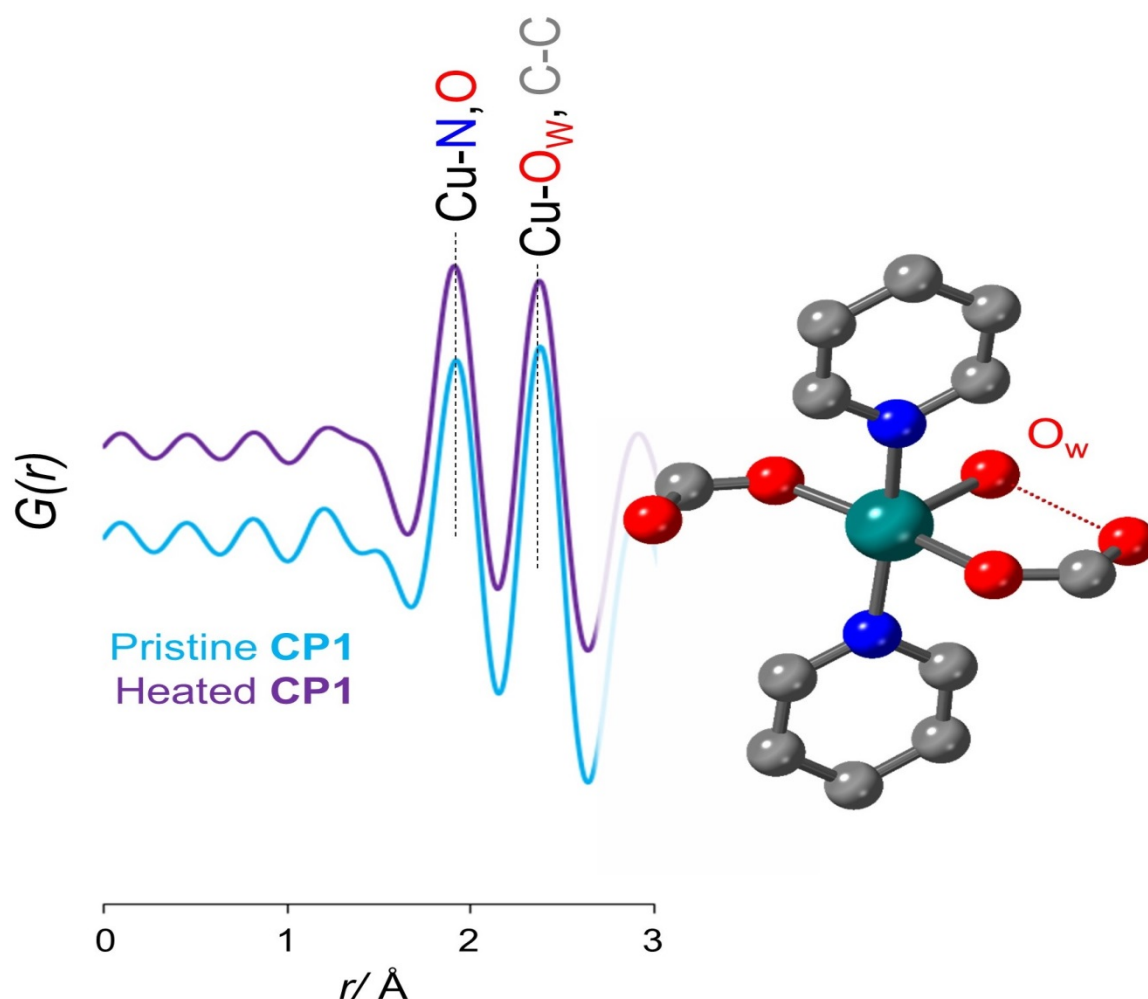


Figure 5. Experimental PDFs for **CP1** (pristine) and **CP1-H₂O** (heated) samples before and after heating at 60 °C, indicating the two peaks linked to the binding of the 4,4-bipy and TAcO ligands (~ 2.0 \AA) and the water molecule (~ 2.3 \AA). In dash line in the structure indicates, hydrogen bonding between the water molecule and one oxygen atom of the TAcO ligands.

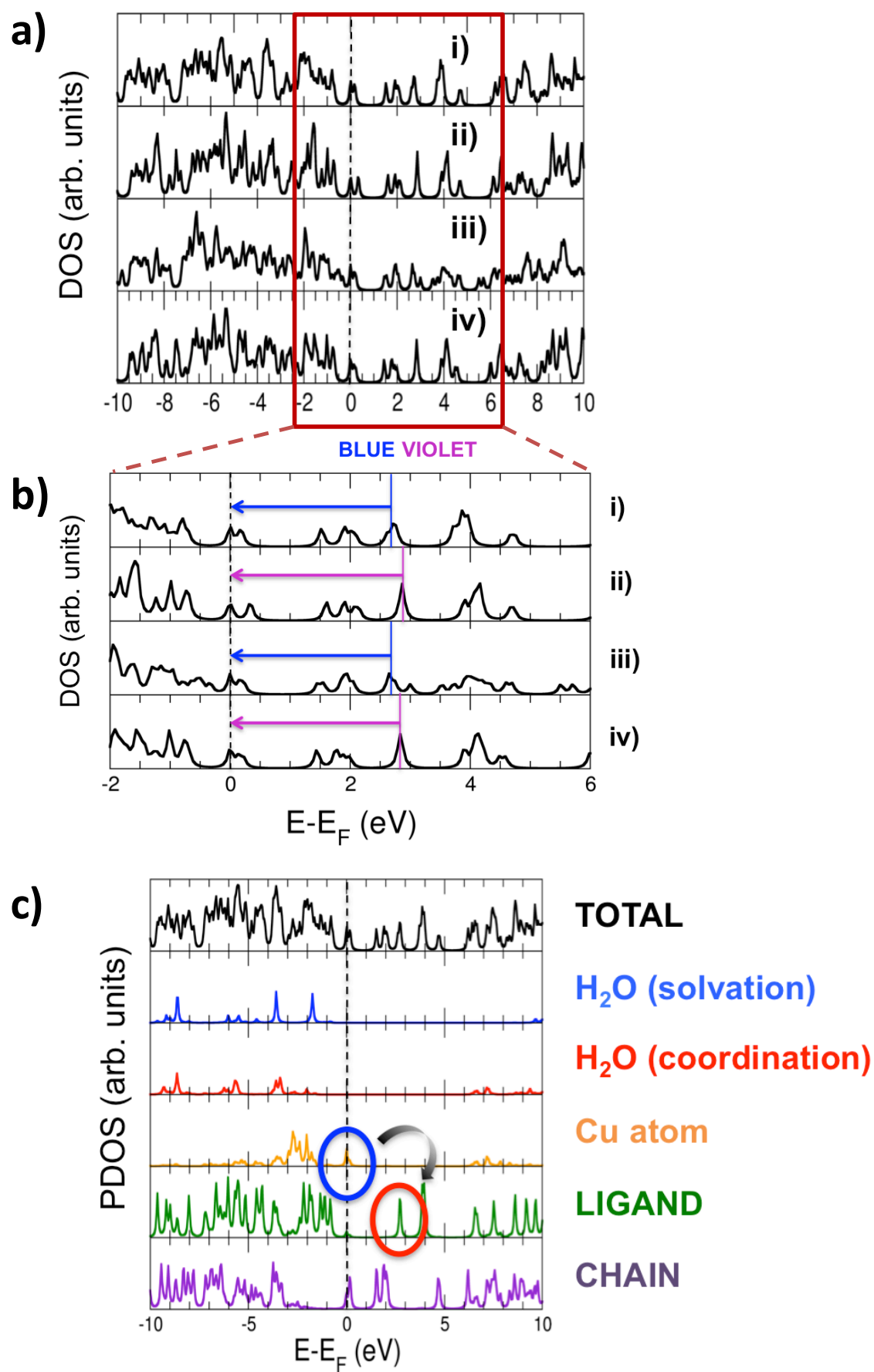


Figure 6. (a) Computed total density of electronic states (DOS, in arb. units) as a function of the energy referenced to the Fermi energy (in eV) for the **CP1** compound: i) with all the coordinated and solvation water molecules, ii) just with the two solvation water molecules, iii) just with the coordination water molecules and iv) with no water molecules. (b) DOS profiles of panels ai-iv) shown in a reduced energy window between -2 and 6 eV; low-lying optical transitions are indicated in blue and violet colors according to their corresponding energy. (c) Computed density of electronic states for the case a.i) projected onto the solvation water molecules, the coordination water molecules, the Cu atoms, the full ligand and onto the full structural chain (Cu atom + 4,4'-bipyridine units); the two electronic states involved in the first permitted optical transition lying within the visible (Cu atom \rightarrow ligands) are highlighted by colored ovals.

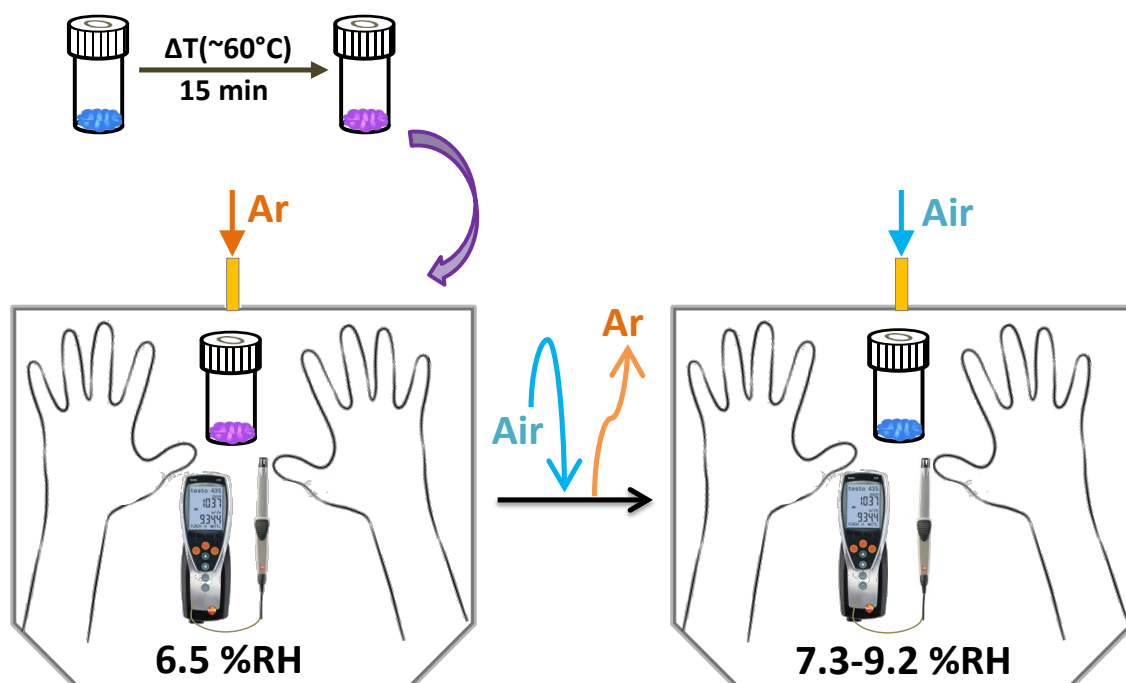


Figure 7. Outline of the experiment carried out in a dry box at 25 °C to detect the capacity of the **CP1-H₂O** as a sensor of relative humidity of the air.

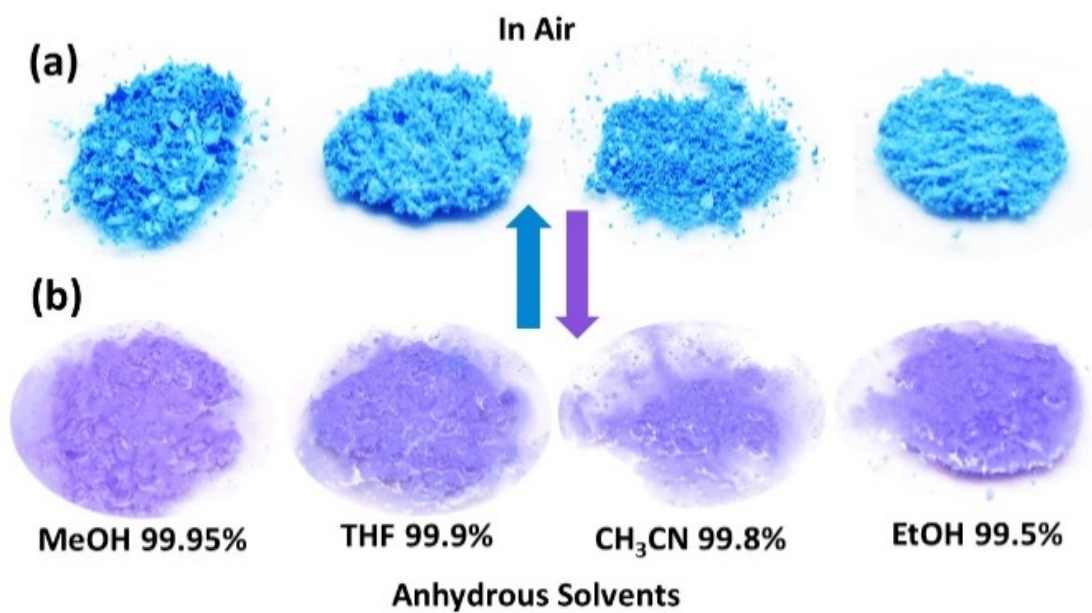


Figure 8. (a) Photos of **CP1** in air. (b) **CP1** after soaking for 1-5 min in different dry organic solvents.

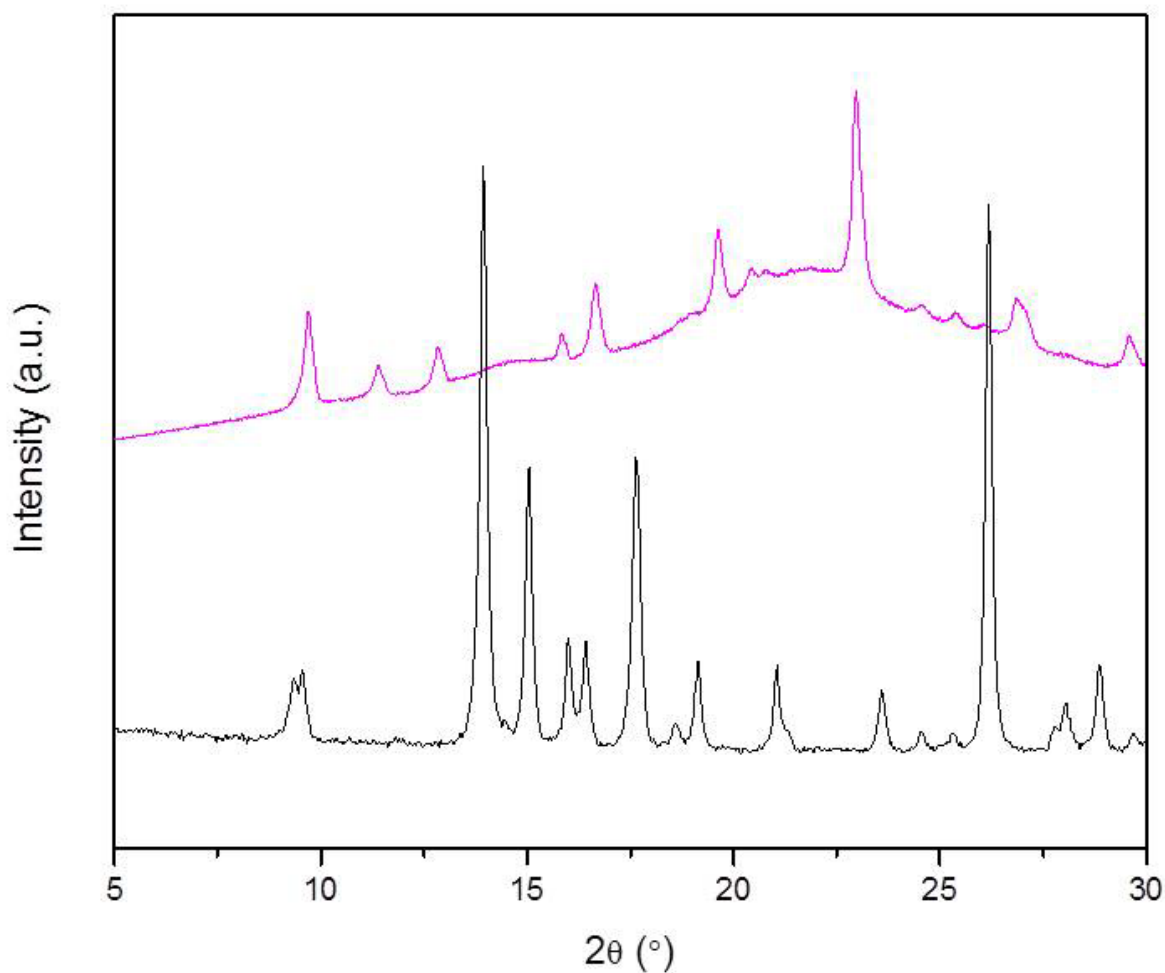


Figure 9. X-ray powder diffraction patterns of **PC1** at 25 °C (black line) and the same compound after soaked in dry EtOH (violet line).

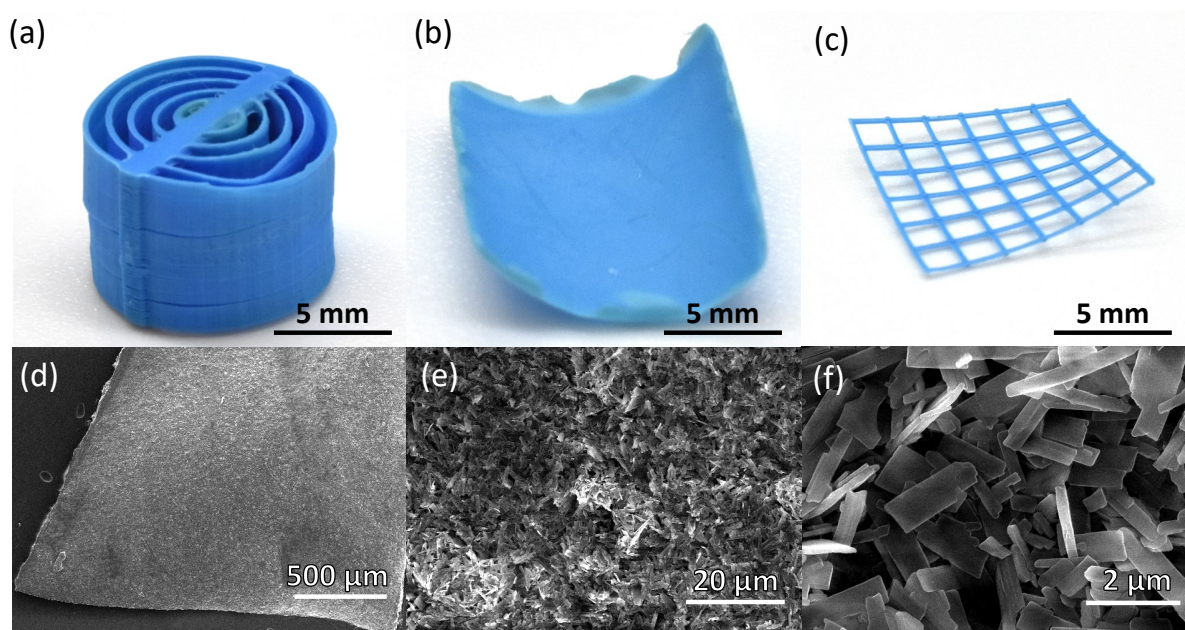


Figure 10. (a-c) Different 3D printed **CP1@3D** architectures. (d-f) Scanning Electron Microscopy (SEM) images of the 3D-printed by extruding printer, **CP1** crystals with the polymeric matrix (**CP1@3D**). The SEM of the 40%wt **CP1** sample.

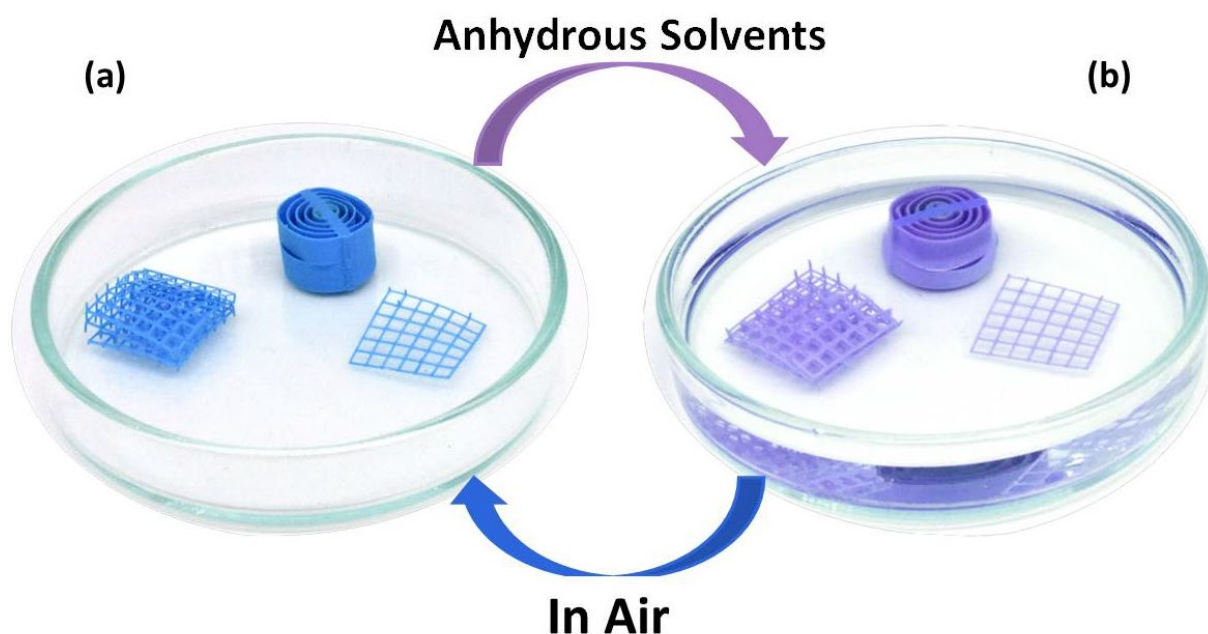


Figure 11. (a) Different architectures of the 3D printed material **CP1@3D** in air at 25 °C, blue color. (b) **CP1@3D**, introduced in dry solvents such as ethanol, methanol, tetrahydrofuran or acetonitrile showing the characteristic violet color.

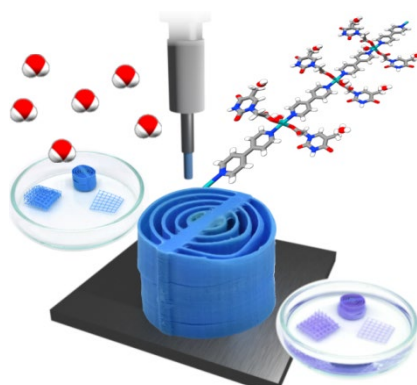
Table 1. Data obtained from the water detection limits (LOD) of **CP1** and 3D printed material (**CP1@3D**) in the presence of different dry solvents.

Solvent	Solvent Aliquot (mL)	CP1 Weight (g)	Water volumen added (mL)	CP1 LOD (%)	CP1@3D Weight (g)	Water volumen added (mL)	CP1@3D LOD (%)	CP1-H ₂ O Weight (g)	Water volumen added (mL)	CP1-H ₂ O LOD (%)
MeOH 99.95%	2	0.0040	0.085	4.7	0.0098	0.085	4.8	0.0086	0.11	6.0
EtOH 99.5%	2	0.0036	0.02	1.7	0.0084	0.01	1.0	0.0084	0.05	3.2
THF 99.9%	5	0.0097	0.01	0.3	0.0084	0.015	0.4	0.0082	0.02	0.5
ACN 99.8%	5	0.0043	0.01	0.4	0.0118	0.01	0.4	0.0085	0.02	0.7

This work opens the door to generate new 3D printed materials based on the integration of multifunctional coordination polymers with organic polymers. The fabrication of 3D printed composite objects based on Cu(II) coordination polymer, with utility as a water colorimetric sensor is presented. The sensing capacity is related with the loss of water molecules with temperature or by solvent molecules competition.

Keywords: coordination polymers, sensing, 3D printing, solvato-thermochromic, water detection

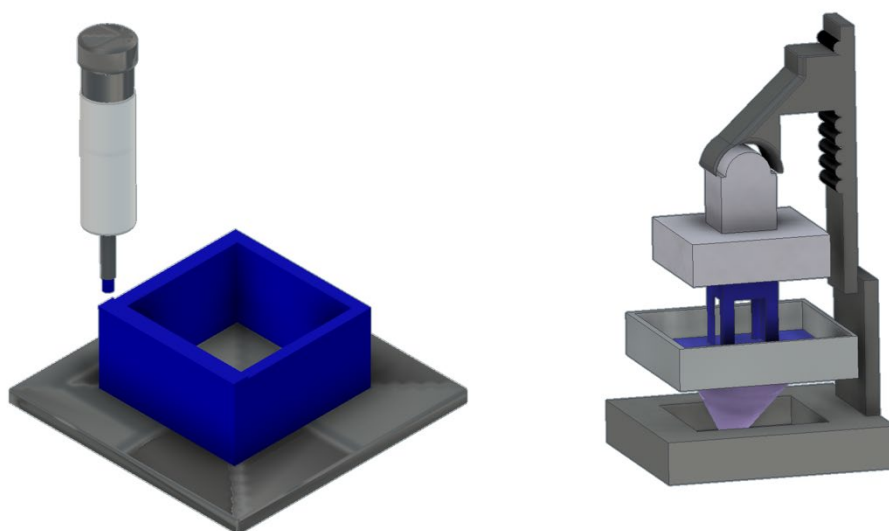
3D printing of a thermo- and solvato-chromic composite material based on a Cu(II)-thymine coordination polymer with moisture sensing capabilities



Supporting Information

3D printing of a thermo- and solvato-chromic composite material based on a Cu(II)-thymine coordination polymer with moisture sensing capabilities

Noelia Maldonado, Verónica G. Vegas, Oded Halevi, Jose Ignacio Martinez, Pooi See Lee Shlomo Magdassi, Michael T. Wharmby, Ana E. Platero-Prats, Consuelo Moreno, Félix Zamora and Pilar Amo-Ochoa**



Scheme S1. Operating scheme of a Digital Light Processing (DLP) printer. (a) Extruder 3D-printer (Hyrel System 30M). (b) Digital light processing (DLP) 3D-printer (Asiga Pico2)..

Its thermal study (**Figure S1**), shows a 1st stage at 60 °C probably indicative of the loss of one coordinated water molecule (obsd 2.58%, calcd 2.75%, the ionic current indicates that there is only water). At 135 °C we can observe a 2nd stage also indicative of the loss of probably two lattice solvation water molecules (obsd 5.47%, calcd 5.62%). The observed values are somewhat different than those calculated. However, in several DTA-TG experiments these values always differ slightly, which can be regarded to the preparation of the material.^[16] From 140 °C to 500 °C, the next stages correspond to the loss of organic ligands, TAcO and 4,4'-bipy, as CO₂ and H₂O gas.

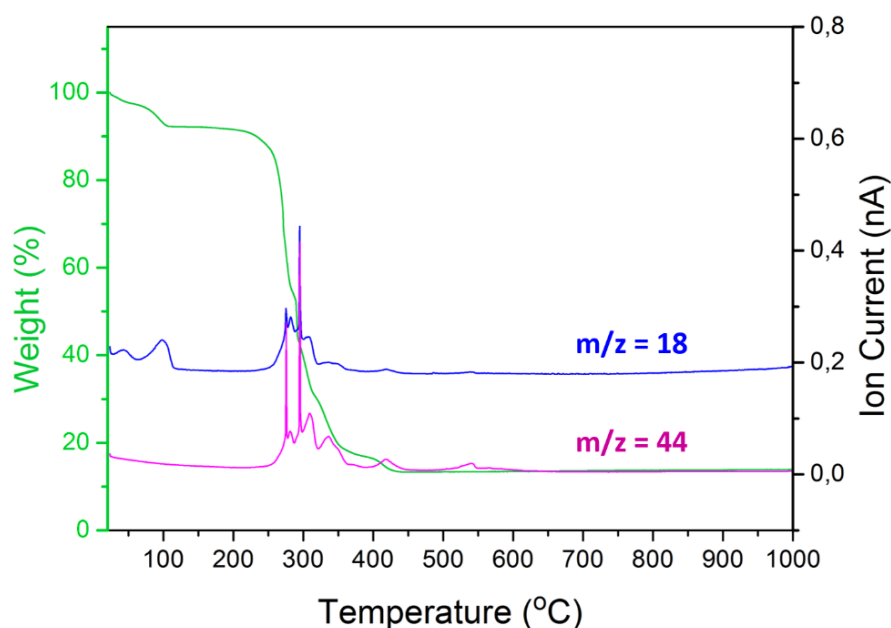


Figure S1. Thermal stability study of **CP1**. Signs of the thermogram: Green curve: represents the stages of the losses produced. Blue and pink curve: represent the ion currents corresponding to the masses 18 (blue) and 44 (pink) associated with each loss of the previous curves. Only those two are represented from a range of 0 to 200 u.m.a because there are no more significant signals.

In addition, DSC measurement, (**Figure S2**) was performed to clarify the order in which the water molecules leave the **CP1**, looking for a substantial difference in the bond breaking energies of the dehydration reaction and the possibility to obtain extra information from the structural change that occurs at 135 °C. For it, two assays were realized at different heating rates, (5 and 10 °C/min) from room temperature to 200 °C. It observes (Figure S2) that the first thermal event coincides with the TGA first step and this enthalpy is less than the second thermal event which also coincides with the TGA second step. These events occur at different temperatures depending on the heating rate, indicating the lability of the bond in the coordination water molecule.

However, these data don't allow to distinguish what molecules of water leave first, because the shape of the second event peak and the recovery of the baseline at the end indicate that this phenomenon contains overlapping between the energy of two water molecules loss and the energy reaction when a new structure emerges, which happens when the solvation water molecules are lost and depends on it kinetically and thermodynamically.

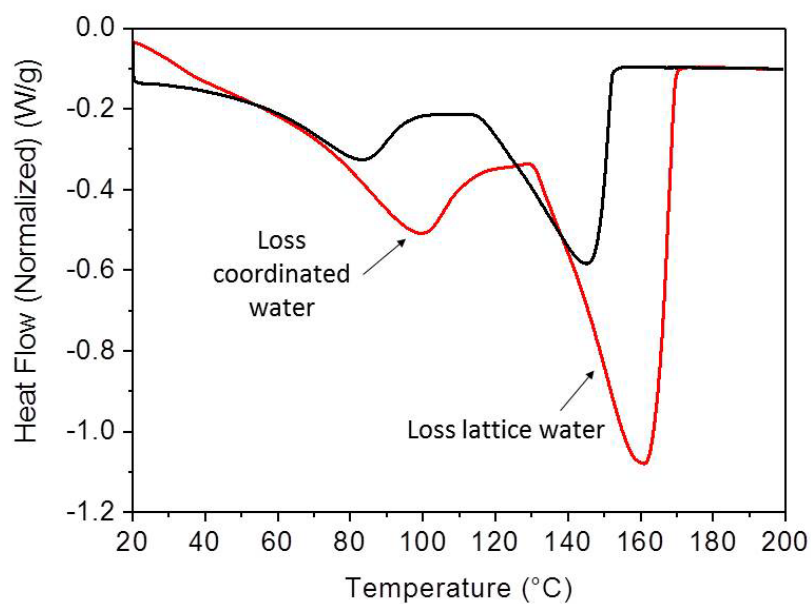


Figure S2. DSC curves of **CP1** at different heating rates.

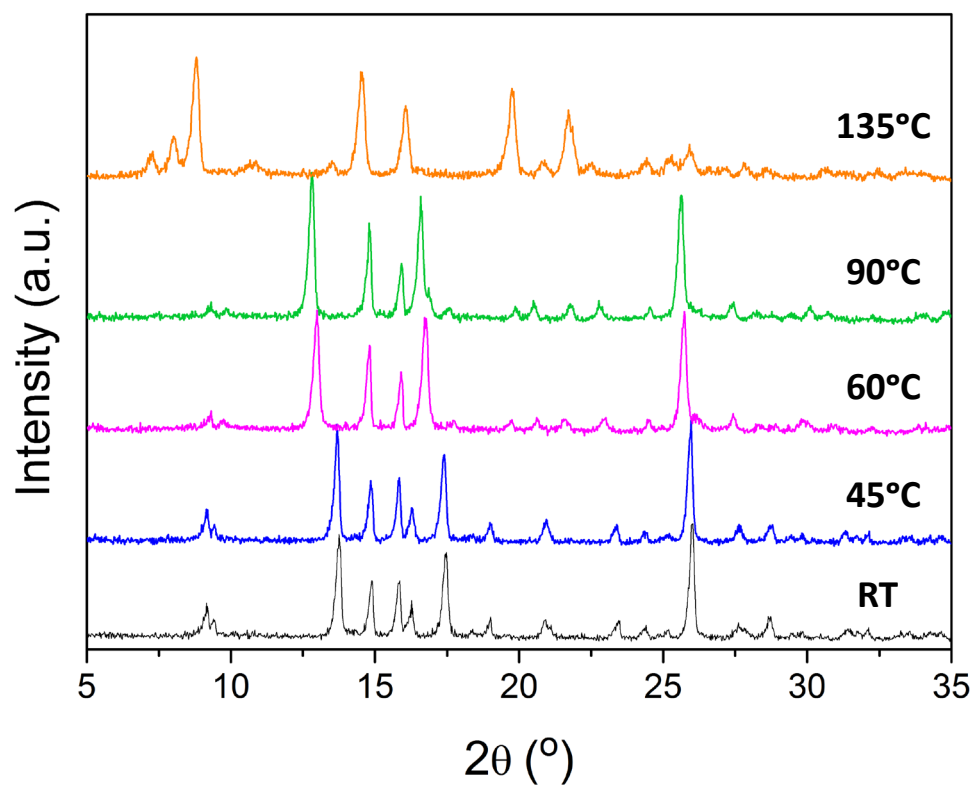


Figure S3. Powder XRD of **CP1** at different temperatures.

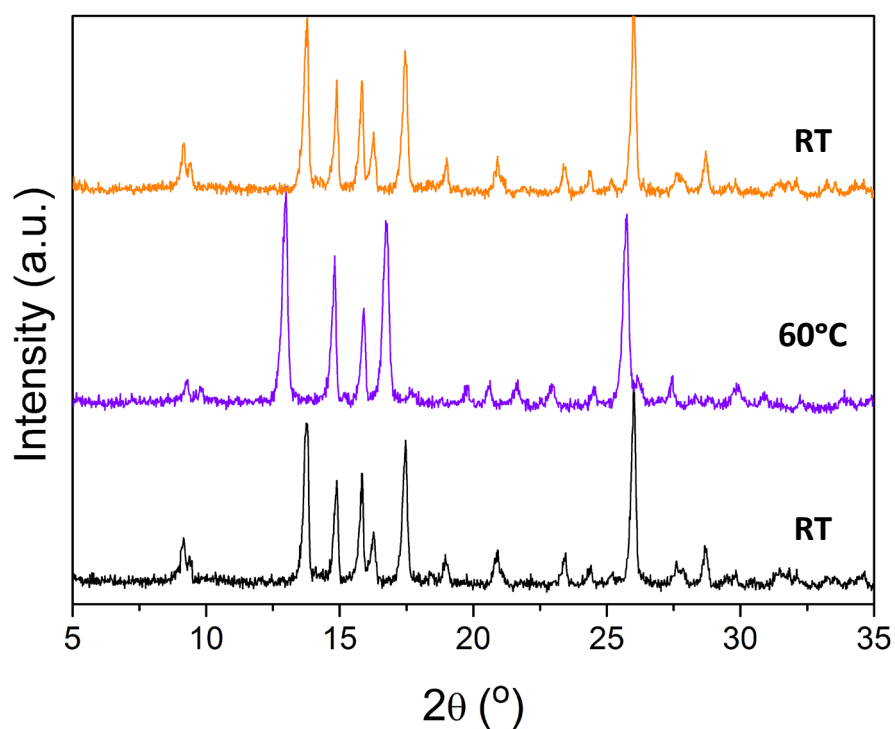


Figure S4. Powder XRD of **CP1** (black line) and **PC1-H₂O** (purple line) and the reversibility process (orange line).

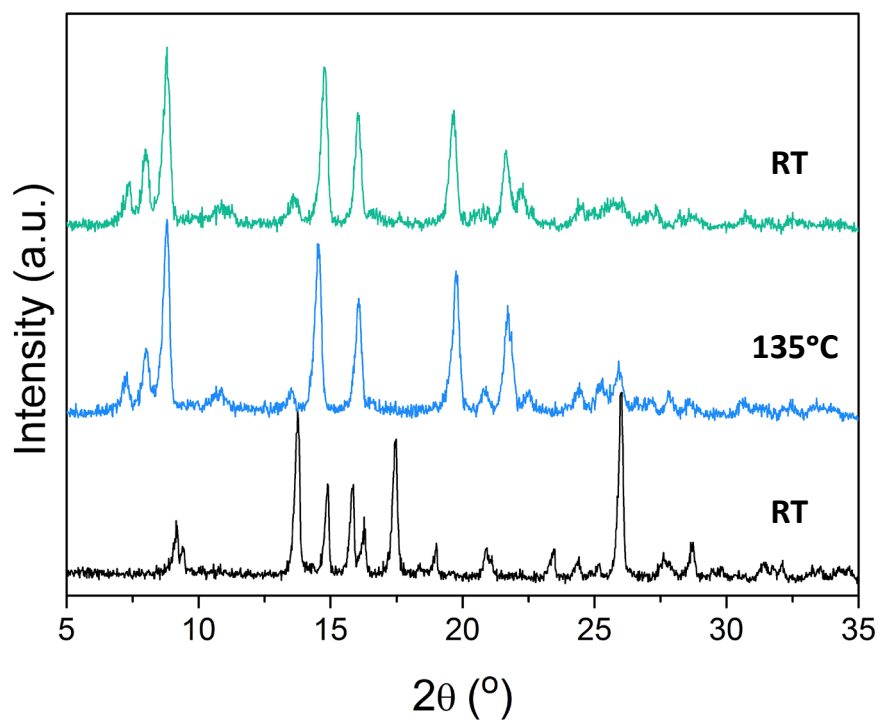


Figure S5. Powder XRD of **CP1** at 25 °C (black line) and 135 °C (blue line) showing the irreversibility of this process (green line).

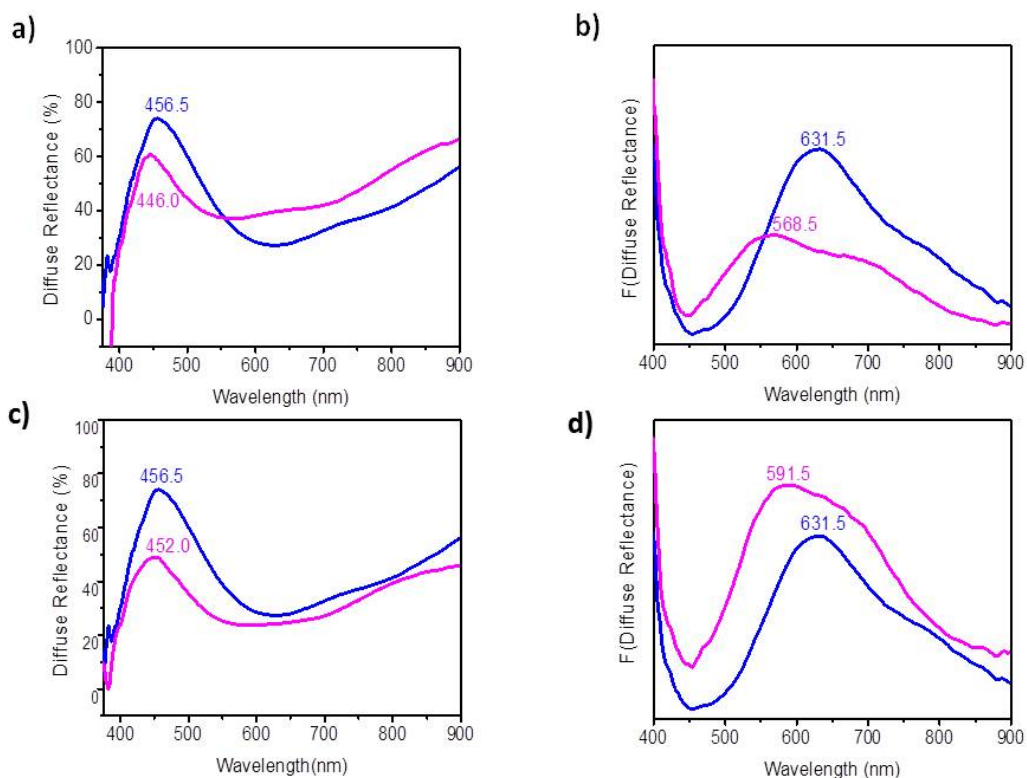


Figure S6: Diffuse reflectance (**a, c**) and the Kubelka-Munk (**b, d**), remission function spectrum obtained for **CP1**, before (initial, blue line) and after (final, violet line) be heated at 66.6 °C (**a** and **b**) and before (initial, blue line) and after (final, violet line) be immersed in dry methanol (MeOH) at 25 °C (**c** and **d**).

		Maximum Wavelength of Diffuse Reflectance (nm)		Maximum Wavelength of Kubelka-Munk (nm)	
	Change	Initial	Final	Initial	final
CP1	MeOH	456.5	452.0	631.5	591.5
CP1	66.6 °C	456.5	446.0	631.5	568.5

Table S1: Comparison of maximum wavelengths of both, the diffuse reflectance spectra and the Kubelka-Munk remission function of **CP1**, before (initial) and after (final) heating at 66.6 °C and before (initial) and after (final) being immersed in dry methanol (MeOH) at 25 °C.

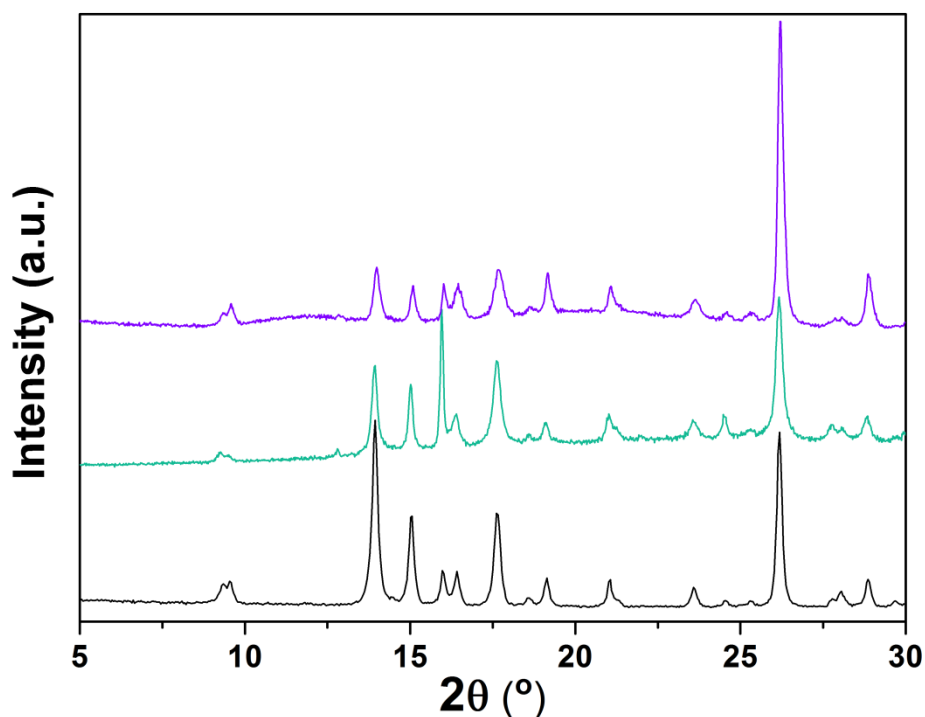


Figure S7. Simulated **CP1** (black line), experimental **CP1** (green line) and printed **CP1@3D** (purple line), X-ray powder diffractograms after 20 cycles applying 60°C and cooling o air.

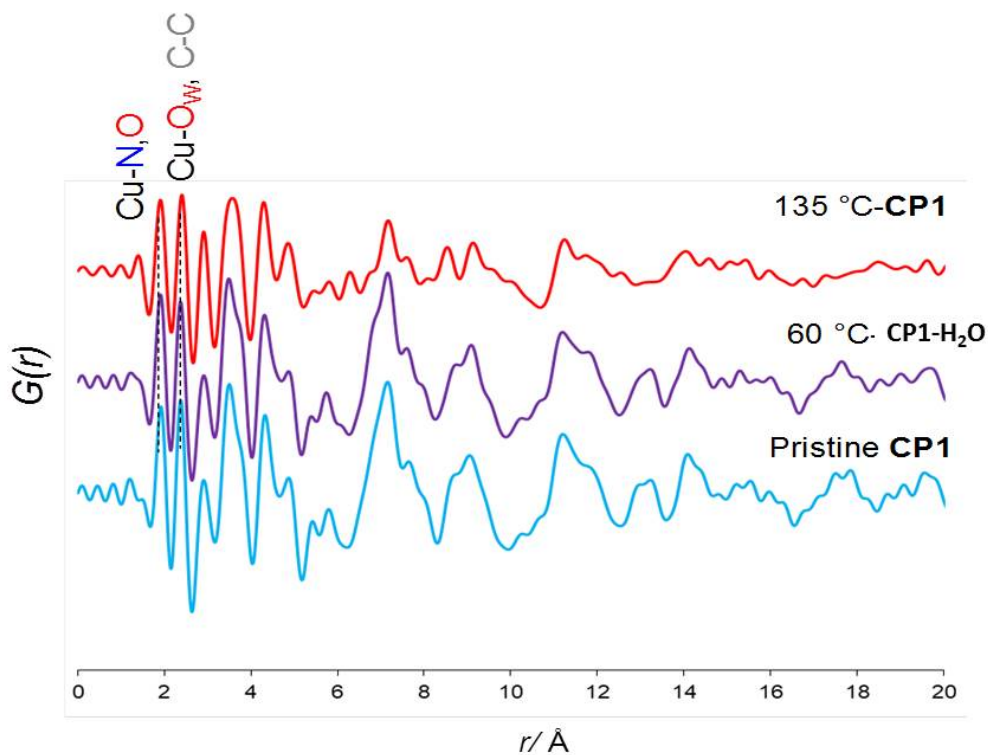


Figure S8. Experimental PDFs for **CP1** samples before and after heating at 60 and 135 °C, indicating the two peaks linked to the binding of the 4,4-bipy and TAcO ligands (~ 2.0 Å) and the water molecule (~ 2.3 Å).

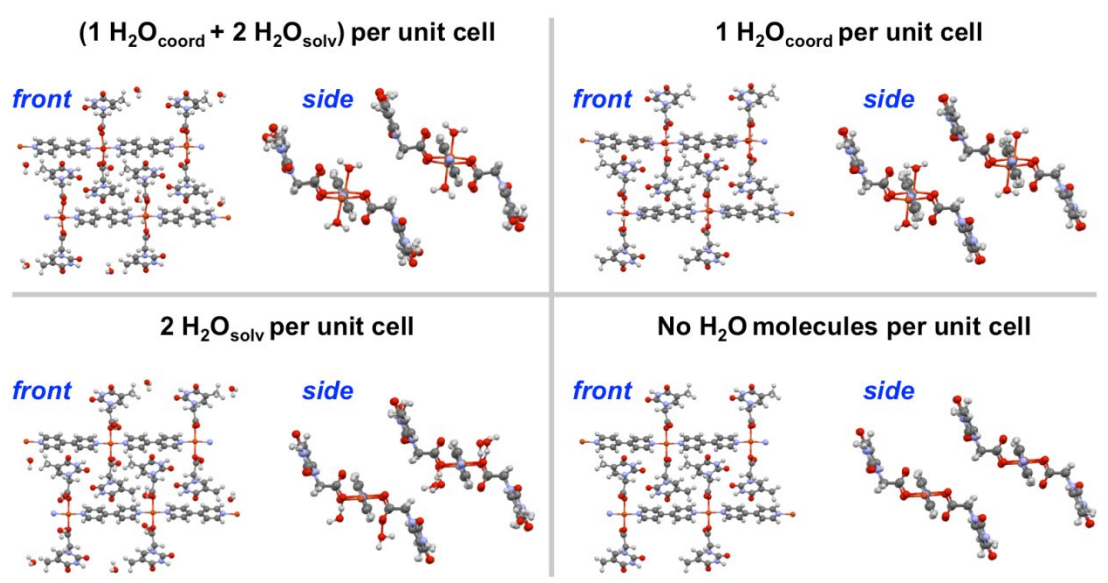


Figure S9. Front and side views of the computed optimal geometries for the compound **CP1**: (top-left) with 1 coordination and 2 solvation water molecules per unit cell, (top-right) with 1 coordination water molecule per unit cell, (bottom-left) with 2 solvation water molecules per unit cell, and (bottom-right) with no water molecules.

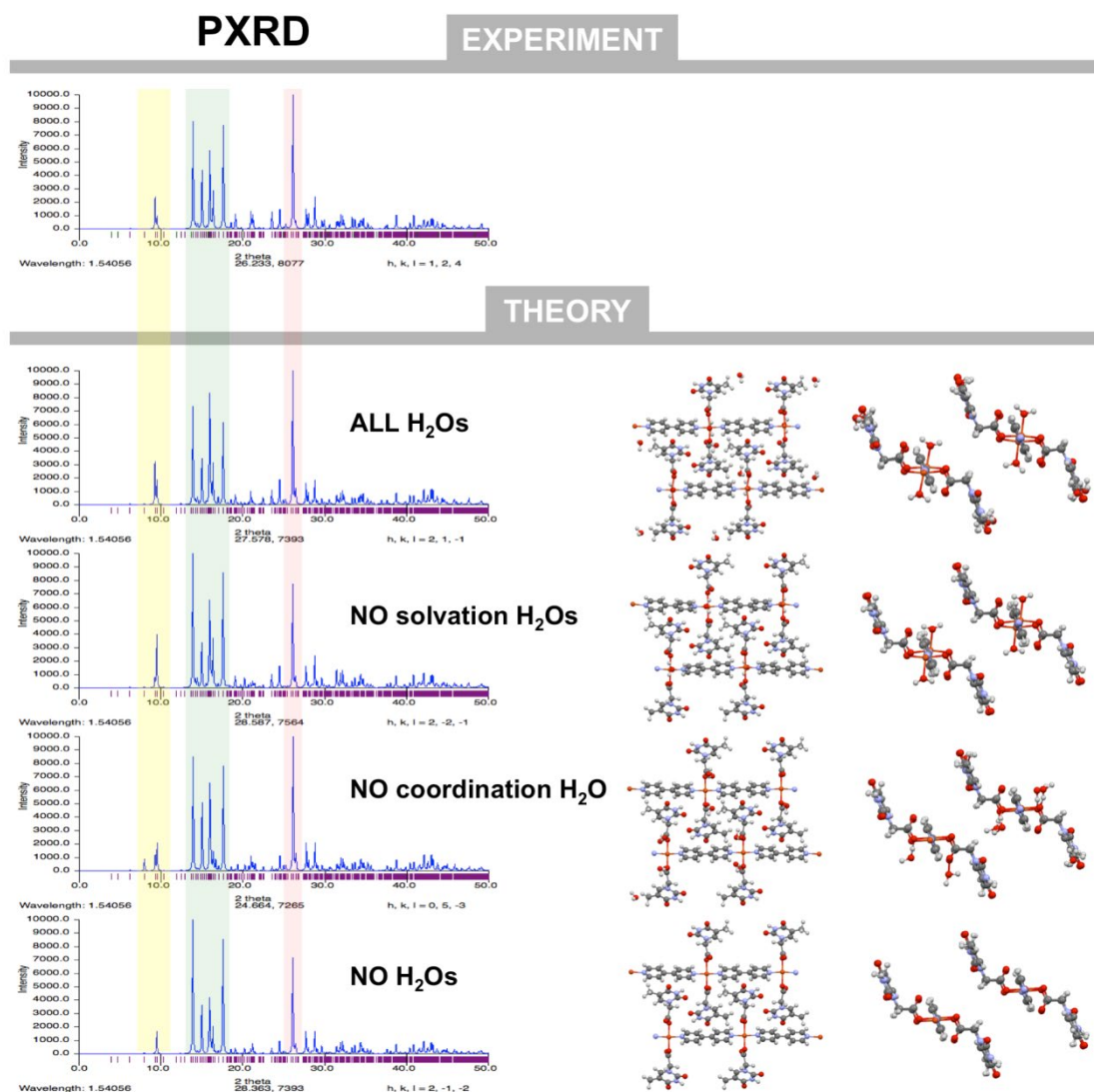


Figure S10. (Top panel) Experimental diffractogram for the **CP1** compound with 1 coordination and 2 solvation water molecules per unit cell. (Bottom panel) Simulated PXRD diffractograms from the DFT-optimized structures; front and side views of the structures have been included for each corresponding diffractogram. Color-shadowed stripes, overlapping all the PXRD spectra, have been also added highlighting the most representative regions.

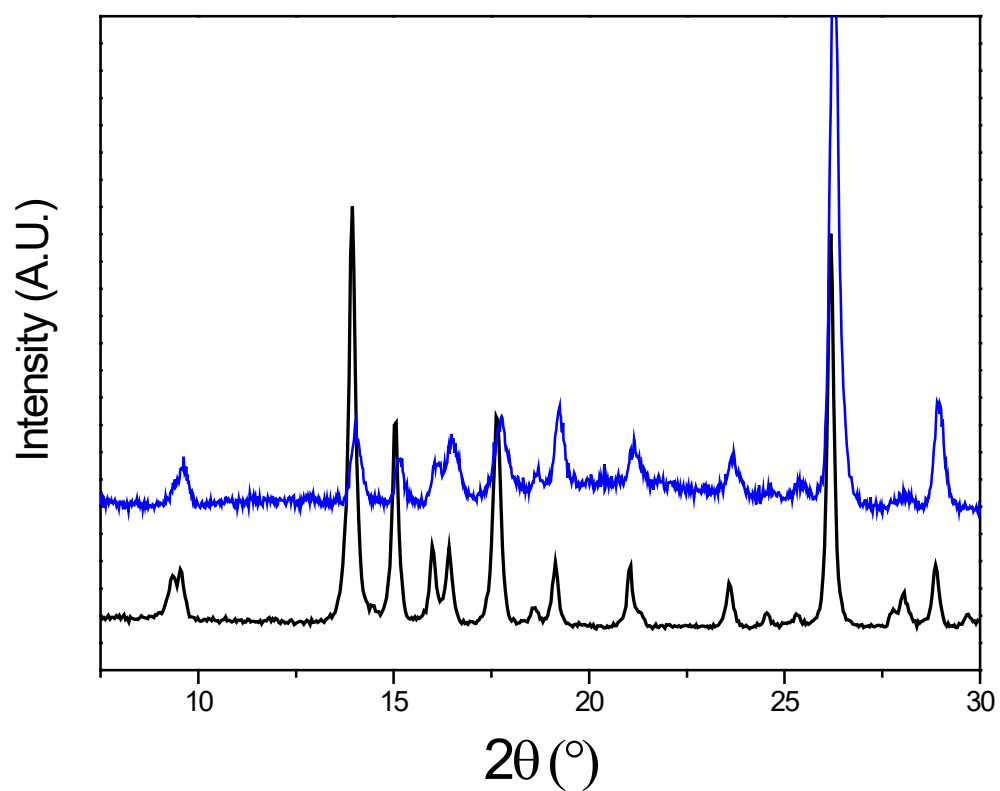


Figure S11. Powder X-ray diffractograms of the powder **CP1** (dark line) and the printed **CP1@3D** (blue line).